UNIVERSITY OF OKLAHOMA

GRADUATE COLLEGE

NUMERICAL SIMULATION OF HYDRAULICALLY INDUCED CASING DEFORMATION IN SHALE RESERVOIR

A THESIS

SUBMITTED TO THE GRADUATE FACULTY

in partial fulfillment of the requirements for the

Degree of

MASTER OF SCIENCE

By

ZIYI XU
Norman, Oklahoma
2018

Downloaded from SHAREOK. Persistent Handle URL: https://hdl.handle.net/11244/301318

NUMERICAL SIMULATION OF HYDRAULICALLY INDUCED CASING DEFORMATION IN SHALE RESERVOIR

A THESIS APPROVED FOR THE
MEWBOURNE SCHOOL OF PETROLEUM AND GEOLOGICAL ENGINEERING

BY

_____
Dr. Xingru Wu, Chair

_____
Dr. Catalin Teodoriu

_____
Dr. Ahmad Jamili

© Copyright by ZIYI XU 2018
All Rights Reserved.

Dedicate to my dear mom and dad who gave me countless love and support.

Acknowledgements

I would like to express my sincere gratitude to my advisor, Dr. Xingru Wu and Dr. Fei Yin – for their numerous guidance and assistance in the process of conducting this research study, and my entire degree program. I appreciate their generous help and extremely patience. It is their support and trust that support me to complete this research. In the past one year, I have been learning from them all the time.

I also would like to acknowledge my committee members, Dr. Catalin Teodoriu and Dr. Ahmad Jamili, for their guidance of my research. Their courses and advices were great help for this research. I am also grateful to Dr. Rouzbeh Moghanloo, Dr. Deepak Devegowda, Dr. Zhen Zhu, Dr. Mashhad Fahes, Dr. Ramadan Ahmed, Dr. Siddharth Misra for their help.

I want to say thank you to my dear friend and roommate Yao Wang for her two years' company, it is awesome to have you sharing all the stories and memories. I also want to say thank you to the best 1337 fellow Kai Wang for his encouragement all the time. His strong sense of responsibility for research and family is respectable. I would also like to appreciate Dr. Liangliang Huang and Jianrong Lu for their earnest and kind technical support. Here I also want to say thank you to Jing Zhang, Guomin Ji, Zhiyi Jing, Jing Fu, Bin Yuan, Jiabo He, Hao Li, Yifu Han, Kang, Da Zheng, Jin Yin, Sangcheol Yoon, Michael, George, Som, Lei Han, Mijin, Jocin, Adonis, Nabe, Raymos, Mansi and all my friends I met in OU. Thank you for giving me so many joys and laughter during this unforgettable time.

Finally, I would like to say thank you to my best parents and friends B&P for everything, love you as always.

Table of Contents

Acknowledgements iv

List of Table vii

List of Figures viii

Chapter 1: Introduction 1

1.1 Motivation and Problem Statement 1

1.2 Objectives 3

1.3 Organization of the Thesis 3

Chapter 2: Literature Review 5

2.1 Fundamental of Hydraulic Fracturing 5

2.2 Hydraulic Fracturing Simulation 6

2.2.1 Mathematical Simulation Models 6

2.2.2 Numerical Modeling Methods 9

2.2.3 Hydraulic Fracture Propagation Mechanisms 10

2.3 Casing Deformation after Hydraulic Fracturing in Shale Formation 10

2.4 Casing Failure Mode 11

2.5 Possible Reasons of Casing Failure 14

2.5.1 Connection with Lithology Discontinuities 18

2.5.2 High Tectonic Stress and High Tectonic Stress Difference 20

Chapter 3: Methodology 23

3.1 Introduction of Methods to Simulate Hydraulic Fracturing in Abaqus 23

3.2 Rock Elastic Constitutive Relation 24

3.3 Fluid Flow in Cohesive Element 24

3.4 Fluid-Solid Coupled Equilibrium Equation in Formation 26
3.5 Fluid-Solid Coupled Continuity Equation in Formation 27
3.6 Cohesive Zone Method (CZM) 28
3.7 Cohesive Element Initiation 30
3.8 Cohesive Element Propagation 31
3.9 Model Constructions 33
3.10 Model Assumptions 38
3.11 Model Set-up 39
Chapter 4: Case Study 42
4.1 Case Study Well Information 42
4.2 Case Study Input 42
4.3 Case Study Results 43
Chapter 5: Sensitivity Study 54
5.1 Tectonic Stress 54
5.2 Young's Modulus 56
5.3 Fracturing Fluid Injection Rate 57
5.4 Fracturing Fluid Viscosity 59
Chapter 6: Conclusions and Recommended Future Work 61
References 63

List of Table

Table 2.1 Casing selection with deform rate in C-W area. 11

Table 2.2 Lithology discontinuities observation at deform position. 20

Table 2.3 Statistics of tectonic stress in C-W area. 21

Table 4.1 Input parameter for 2D base model simulation 42

Table 4.2 Maximum y-direction displacement changes with time. 53

Table 5.1 Input parameter for 2D base model simulation. 54

Table 5.2 Sensitivity on tectonic stress. 55

Table 5.3 Maximum y-direction displacement under different Young's Modulus. 57

Table 5.4 Slip response under different injection rate. 59

Table 5.5 Slip situation under different viscosity. 60

List of Figures

Figure 1.1 Casing deformation rate with develop stages in C-W area. 2

Figure 1.2 Technical route. 4

Figure 2.1 Complex fracture system after fracturing operation. 6

Figure 2.2 The KGD fracture model. 7

Figure 2.3 The PKN fracture model. 8

Figure 2.4 Pseudo 3D model. 9

Figure 2.5 Earthquake induced overburden shear damage. 12

Figure 2.6 Photo of lead impression in C-W area. 13

Figure 2.7 Multi-arm caliper well log image. 13

Figure 2.8 Schematic of casing shear deformation. 13

Figure 2.9 Possible reasons of casing deformation. 15

Figure 2.10 Micro-seismic map of a well in C-W area during fracturing. 16

Figure 2.11 Schematic of possible geomechanics causes. 18

Figure 2.12 Well log data of X well in C-W area. 19

Figure 2.13 Three types of stress regimes. 21

Figure 2.14 Diagram of strike-slip and thrust faults 22

Figure 3.1 Flow within cohesive element. 25

Figure 3.2 Cohesive traction-separation constitutive relation. 30

Figure 3.3 Schematic model of 3D finite element model of casing in slip rock. 34

Figure 3.4 Casing Von Mises stress distribution under various slip displacements. 34

Figure 3.5 Schematic diagram of natural fracture slip induced slip. 36

Figure 3.6 3D schematic of fractures and wellbore. 37

Figure 3.7 Fracture model assumption. 37

Figure 3.8 Schematic of simplification from 3D model to 2D model. 38

Figure 3.9 Finite element model with mesh. 40

Figure 3.10 2D model of fractures and wellbore. 41

Figure 4.1 Fracture propagation trace at different time. 44

Figure 4.2 Cloud graph of y-direction displacement before intersection. 46

Figure 4.3 Vector graph of y-displacement during intersection at 451.7 s. 47

Figure 4.4 Cloud graph of y-direction displacement at 603 s after intersection. 48

Figure 4.5 Vector graph of y-direction displacement at 603 s. 48

Figure 4.6 Maximum y-direction displacement change with time. 49

Figure 4.7 Maximum y-direction displacement before slip. 50

Figure 4.8 Maximum y-direction displacement after slip. 50

Figure 4.9 X-direction displacement along horizontal well before slip. 51

Figure 4.10 X-direction displacement along horizontal well after slip. 52

Figure 4.11 Y-direction displacement along horizontal well before slip. 52

Figure 4.12 Y-direction displacement along horizontal well after slip. 53

Figure 5.1 Influence rule of tectonic stress difference on slip displacement. 56

Figure 5.2 Maximum y-direction displacement and YMS relation curve. 57

Figure 5.3 Slippage initiate time with injection rate. 58

Figure 5.4 Maximum y-direction displacement under different injection rate..... 59

Figure 5.5 Maximum y-direction displacement under different viscosity. 60

Abstract

Hydraulic fracturing stimulation is widely conducted to enhance hydrocarbon production in low-permeability reservoirs. However, the massive fracturing can lead to the well failure by compromising well integrity. In this thesis, the mechanism of casing deformation in shale reservoirs during hydraulic fracturing process is studied.

The statistical analyses show that shear slip of weak rock is closely related to casing failure. To investigate the shear slip of rock and its effect on casing deformation, a two-dimensional finite element model (FEM) of injection-induced deformation under hydraulic fracturing is established. The poro-elastic constitutive relation is used to analyze the changes of stress and flow during hydraulic fracturing. In the model, fracture growth is simulated with cohesive zone model (CZM), and the result of slip displacement can be used to predict casing deformation. Lastly, parametric analysis is conducted to show the relationship between different parameters and the formation deformation as well as natural fracture slippage. The fracture slip causes large casing shearing deformation. This study concludes that the shear deformation induced by the slippage of shear fractures during hydraulic fracturing have a big influence on casing integrity and can be inferred as a major casing failure mechanism.

In the casing deformation mechanism study, this work quantitatively predicts the rock slippage during fracturing under various conditions using finite element models. The findings can be used to forecast formation/wellbore response and casing deformation under hydraulic fracturing, which supplies technique support for safe and effective shale gas development.

Chapter 1: Introduction

1.1 Motivation and Problem Statement

The advancement of drilling and fracturing techniques made it technically possible and economically viable to develop extremely low permeability gas and oil reservoirs. The hydrocarbon development from tight formations is a game changer which not only satisfies the domestic energy in US, but also changes US from an oil and gas importer to exporter. China is also abundant in technically recoverable shale resources with a 1,115 Tcf (trillion cubic feet) of gas resources and 32 billion barrels of oil resources (Kuuskraa, Stevens et al. 2013). However, compared with US shale basins, the geology features of shale deep burial, complicated structure and strong anisotropies in China shale formation make the exploration and development more challenging. A particularly challenge facing the shale gas development is casing deformation observed during hydraulic fracturing. C-W shale formation in China is one of the most promising region in China for shale gas development. However, from the start of shale development in C-W shale formation, this region showed a high rate of casing deformation rate as shown in Figure 1.1. Before 2011, the deformation rate was as high as 50%. After several years of operation adjustment and reservoir depletion, the damage rate has been gradually declining even through it is still at a high level, which has been leading to huge loss of production and economy in field. The purpose of this research is to investigate the casing deformation problem induced by hydraulic fracturing in horizontal segments due to shear deformation.

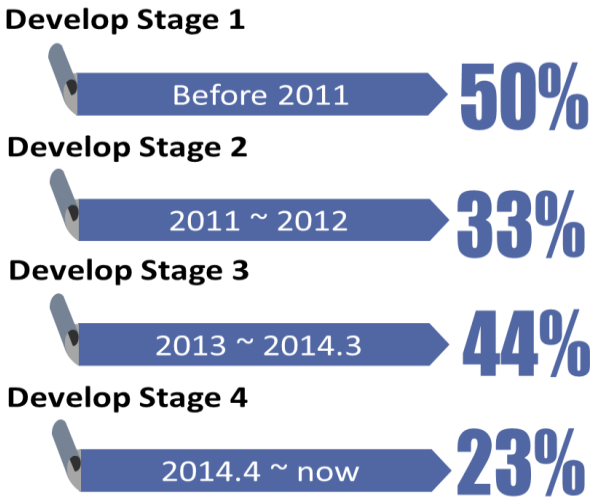


Figure 1.1 Casing deformation rate with develop stages in C-W area.

Shale oil and gas formations usually have low porosities (2% to 6%) and extremely low permeabilities on the order of 0.001 millidarcy to 0.0001 millidarcy (Kuuskraa, Stevens et al. 2013). The mineral compositions of shale contain clay minerals, calcium and silicon minerals. In general, shale reservoirs have no or low natural capacity to produce. To achieve an economic production rate, hydraulic fracturing is needed to improve system conductivity and increase contact area with matrix of shale formation. On one hand, hydraulic fracturing helps achieve a better connection and high flow capacity in shale formation. On the other hand, hydraulic fracturing complicates the casing loading and unloading, which increases the risk of casing failure or compromises wellbore integrity. Even with many observations and studies on casing deformation in shale fields, the mechanism of casing deformation is not well understood. The need of how to maintain well integrity are becoming urgently to be addressed. For this intention, this thesis aims to study the casing deformation mechanism and propose a model to analyze field data using numerical simulation.

1.2 Objectives

The main objective of this thesis is to study the casing deformation mechanism using numerical methods. Before developing a model to simulate casing deformation, the potential influencing factors need to be concluded from the field data analysis. Based on these field data, a simulation model describing the feature of influencing factor can be established for sensitivity studies on uncertainties of subsurface parameters.

1.3 Organization of the Thesis

Chapter 1 is an introduction of basics of hydraulic fracturing and mathematical models used for describing hydraulic fractures.

Chapter 2 provides literature review of previous research on casing deformation and concludes the influencing factors through field data statistical analysis of the deformed wells in C-W area.

Chapter 3 contains modeling methodology and case study. After model setting up, cohesive zone method (CZM) is used to describe hydraulic fracture and natural fracture in model.

Chapter 4 is a case study with the field data of W2X well. The case study is conducted to study slip displacement in fracturing.

Chapter 5 covers the sensitivity study on potential influencing factors in this model, which helps propose future production optimization advices.

Chapter 6 is the conclusion of this study and future work recommendations.

This thesis consists of two major parts: the first is about potential influencing factors of casing deformation, and the second is the model analysis of hydraulic fractured

horizontal wells. To better understand the frame of this thesis, the technical route of this thesis is as provided in Figure 1.2.

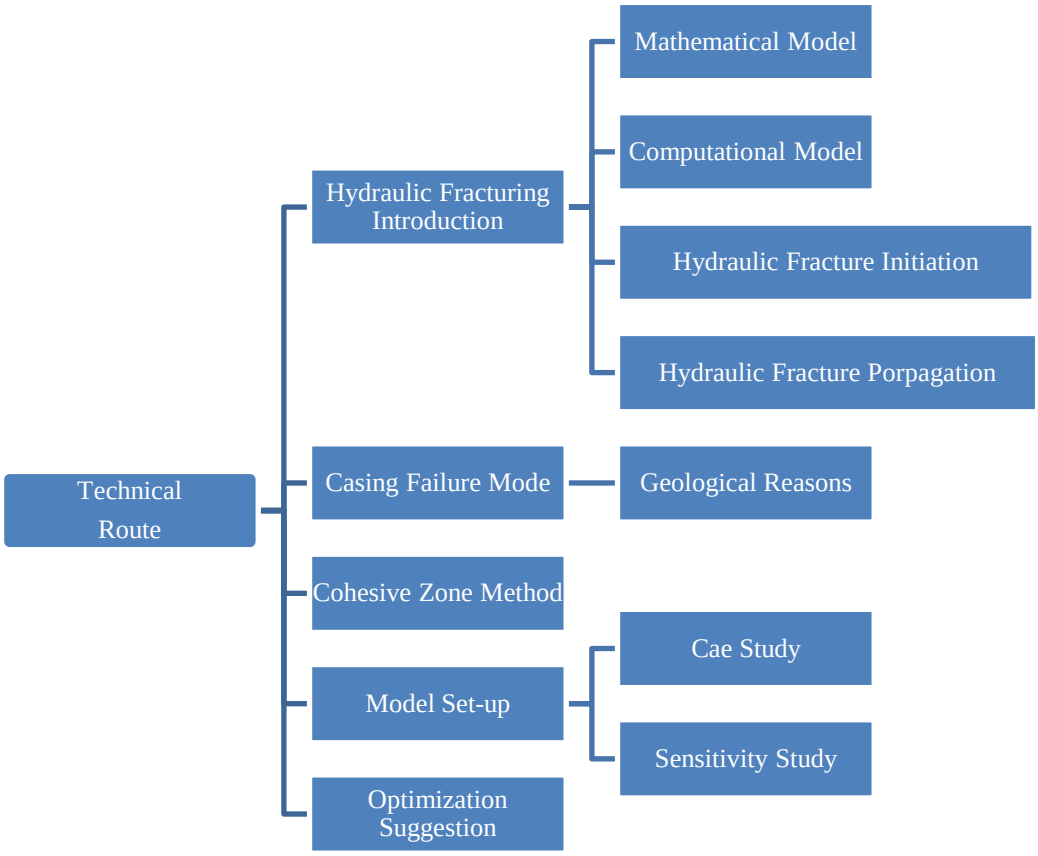


Figure 1.2 Technical route.
This figure describes the structure when build this thesis. The introduction of hydraulic fracturing gives a background of this study, the analysis of casing failure mode is the basis of model build-up, and the cohesive zone method is the methodology of model. Based on case study and sensitivity study, further recommendation for future field operation can be given.

Chapter 2: Literature Review

This chapter covers studies related to casing failure in shale to propose a simple and clear model in explain the mechanism of casing deformation.

2.1 Fundamental of Hydraulic Fracturing

US started the development of shale gas in 1821 and the government has been actively promoting the development of commercial shale plays from the 1976 (EIA). After 30 years' technology development and experience accumulation, hydraulic fracturing has proven to be the key method of effectively developing shale formation.

Hydraulic fracturing refers to pumping a large amount of pressurized fluid slurry containing base fluid and chemicals into the target formation to overcome rock tensile strength (Council 2009). Fractures are generated during the fracturing process to create flow pathways for oil and gas. When the fracture length reaches to the designed extent (from dozens to hundreds of meters), fracturing fluid mixed with proppants will be pumped to keep fractures open. In the early production stage, part of the fracturing fluid is circulated out to surface and leave proppants inside the created fractures. Besides, the pre-existing natural fractures will connect with the induced hydraulic fractures to form a complex fracture network system which further improves the shale reservoir deliverability. Figure 2.1 shows a fracture system in shale after hydraulic fracturing treatment.

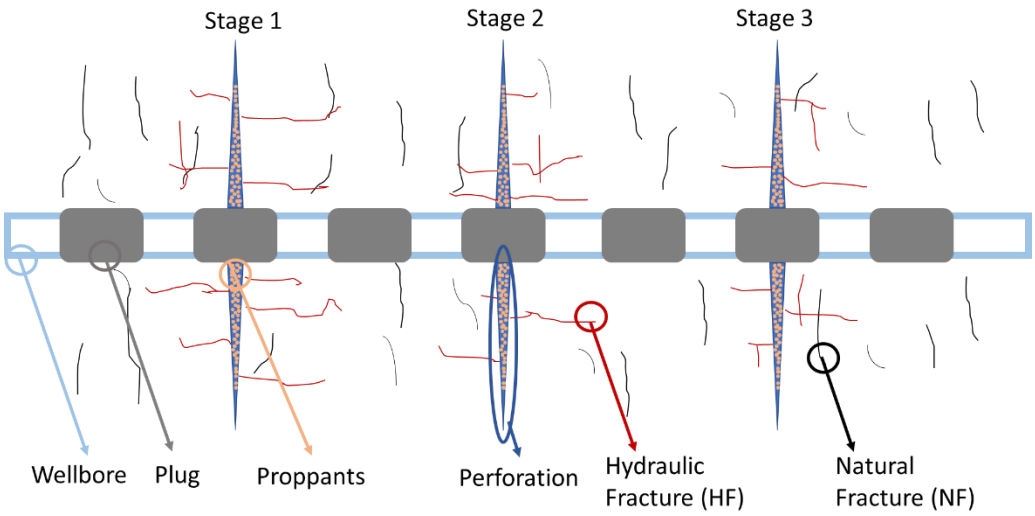


Figure 2.1 Complex fracture system after fracturing operation.
The light blue rectangle block represents the horizontal wellbore, the grey blocks are plugs, the orange particles are proppants in fractures, the dark blue triangle shape represents perforation, the red line demonstrate induced hydraulic fracture (HF), and the black line is pre-existing natural fracture (NF).

2.2 Hydraulic Fracturing Simulation

Hydraulic fracturing is a multiphysics problem containing rock deformation, hydraulic fracture initiation and propagation, hydraulic fracture and natural fracture intersection, natural fracture activation and propagation, fluid flow in pores and fluid leak off into formation. The heterogeneity and anisotropy of formation mechanical properties further complicate the fracturing process.

2.2.1 Mathematical Simulation Models

The geometric dimension (length, height, and width) of created hydraulic fractures influence their flow conductivities. To describe hydraulic fractures, single fracture mathematical models describing the fracture geometry from 2D to 3D are briefly described as follows.

(1) 2D Models

The Khristinaovic-Geertsma-de Klerk model (KGD model), and the Perkins-Kem-Nordgren model (PKN model) are the two simplified 2D models. Both models assume a constant fracture height and fracture only propagates along the fracture length direction during fracturing. Besides, in these two models, the fluid flow along height direction is neglected and only the flow along length direction is considered. In simulation, the fracture height is usually assumed to be the pay zone thickness. KGD model is suitable for the case whose length-height ratio is much less than 1, while PKN model is the best for the scenario whose length-height ratio is more than 1 (Geertsma and De Klerk 1969, Nierode 1985). The KGD model is presented in Figure 2.2, while the PKN model is demonstrated as Figure 2.3.

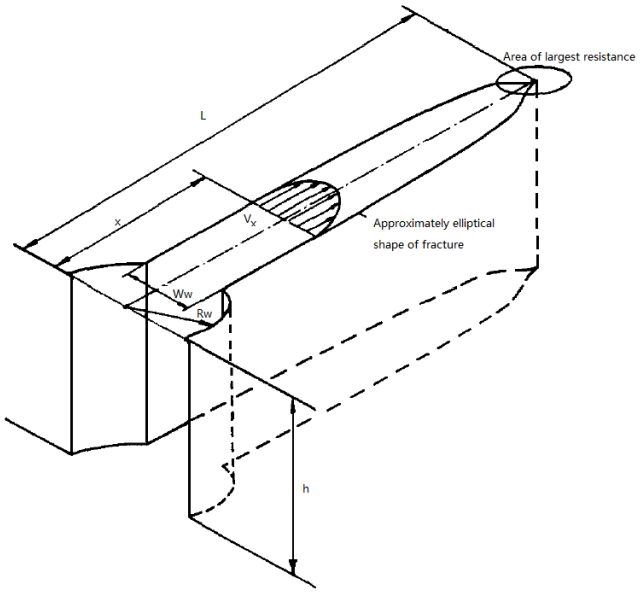


Figure 2.2 The KGD fracture model.
Source: Geertsma and De Klerk (1969). Suitable for the case whose length-height ratio is less than 1.

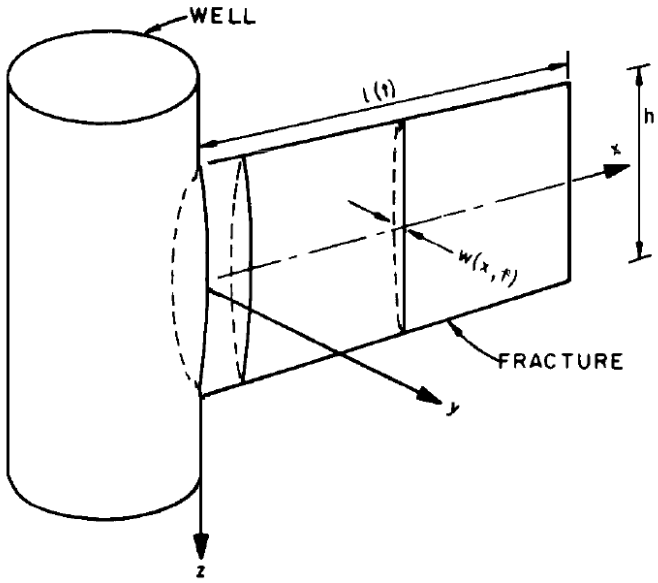


Figure 2.3 The PKN fracture model.
Source: Nordgren (1972). Best for the scenario whose length-height ratio is more than 1.

(2) Pseudo 3D Models (P3D)

In pseudo 3D models as illustrated in Figure 2.4, the fracture height changes with the fracture length grow. The fracture extension is assumed to be an elliptic shape. A 2D deformation and a 1D flow are described by using KGD model to calculate vertical growth and PKN model to calculate horizontal expansion. However, most of the P3D are taking 2D elasticity theory, which is not the reality of rock deform pattern.

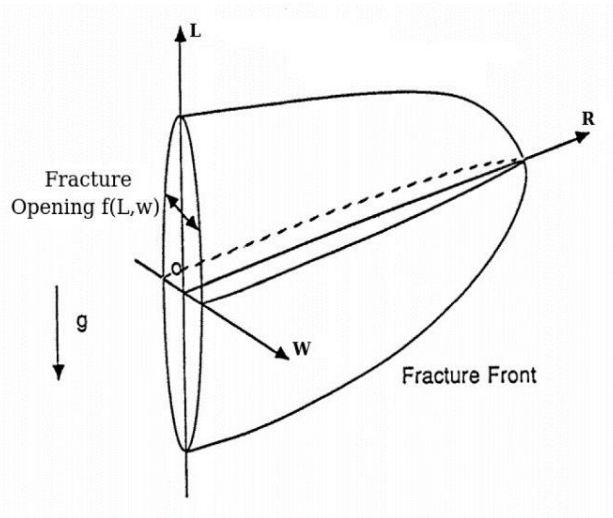


Figure 2.4 Pseudo 3D model.
Source: Nasiri (2015). This model induced description of fracture height growth.

(3) True 3D Model (T3D)

The true 3D model considers fracture extension on both the vertical and horizontal directions and the fluid leak off. A 2D fluid flow along the length and height directions is use in T3D. Since the fracture width is usually much smaller than the fracture length or height, the flow rate along fracture width is usually zero. Therefore, the fluid flow is assumed to be a steady laminar flow and the fracture height increases with the increasing of injection rate.

2.2.2 Numerical Modeling Methods

Many numerical modeling methods of hydraulic fracturing have been developed in literature, and they include: The Finite Element Method (FEM); the Extended Finite Element Method (XFEM) based on continuum mechanics; the Discrete Element Method (DEM) based on non-continuum mechanics; the Boundary Element Method (BEM); the Numerical Manifold Method (NMM); and the Phase Field Method (PFM). Among them, FEM, XFEM, DEM are often used ones.

The FEM (Hughes 2012) can effectively simulate the fracture propagation in heterogeneous and anisotropic rocks by remeshing blocks. Using FEM models, the nonlinear mechanical and complicate stress-strain problems can be solved.

In the XFEM (Moës, Dolbow et al. 1999), the description of discontinuous displacement field is induced and is independent of mesh blocks. Remeshing is no longer required, which reduces the computational cost compared with the FEM.

The DEM (Munjiza 2004) divides the target object into discrete rigid blocks and uses explicit finite difference method to simulate the relationship between rigid blocks. Fractures in DEM can only propagate along rigid block boundaries and can be used to solve discontinuity problems.

2.2.3 Hydraulic Fracture Propagation Mechanisms

The three typical fracture propagation mechanisms are: the Linear Elastic Fracture Mechanics (LEFM), the Elastic Plastic Fracture Mechanics (EPFM), and the Cohesive Zone Method (CZM). Haddad and Sepehrnoori (2015) concluded that the preferred fracture propagation mode for brittle rock is the LEFM, ductile rock is suitable for using the EPFM, and the description for quasi-brittle rock fits best in the CZM. Because the C-W area studying in this research is shale formation, and shale is a type of quasi-brittle rock, so the CZM is used to describe the hydraulic fracture propagation in this study.

2.3 Casing Deformation after Hydraulic Fracturing in Shale Formation

Due to significant changes of stress loading on casing string during massive hydraulic fracturing in shale formation, well barrier or integrity failure should be carefully studied (Davies, Almond et al. 2014). Besides, many field observations have shown that unconventional formations tend to experience higher casing failure rates. In Pennsylvania,

unconventional wells showed a six times higher integrity issue occurring rate compared to the same period conventional wells (Ingraffea, Wells et al. 2014). As denoted in Table 2.1, in C-W area of China, the average casing deformation rate was up to 33.3% in 2011. After applying higher grade of casing, thicker wall, and the optimization of well trajectory, pressure monitor and control, the casing deformation rate dropped to 23.2% during the third develop stage. However, the casing deformation problem remains an unsolved concern. In multi-stage hydraulic fracturing process, the high deformation and failure rate significantly impact the subsequent operations and production efficiency and can even lead to the abandonment of planned interval, which will result in production reduction, formation contamination, and financial loss.

Table 2.1 Casing selection with deform rate in C-W area.

Develop Stage	Outer Diameter（mm）	Grade	Thickness（mm）	Coupling	Deform Rate
1 (Before 2011)	139.7	110/125	9.17/10.54	LTC/BTC	50%
2 （2011～2012）	139.7	TP125V	9.17	TP-BM	33.3%
		P110	9.17	TP-BM	
	139.7	TP95S	9.17	LTC	
	139.7	TP110S	10.54	TP-G2	
3 （2013～2014.3）	139.7	TP140V	9.17	TP-CQ	0%
		VM140HC	12.7	VAM-TOP	
	127	TP140V	12.14	TP-CQ	
	139.7	110	11.1	LTC	57.1%
	139.7		12.14	LTC	
4 （2014.4～2017.6）	139.7	BG125V/Q125	12.7	BGT2	23.2%
				BEAR	

2.4 Casing Failure Mode

Critical casing damage mechanisms observed in a variety of structural settings worldwide include: overburden shear damage on localized horizontal planes (as presented

in Figure 2.5); shearing at the top of production and injection intervals (Rutqvist, Rinaldi et al. 2013); compression and buckling damage within the production interval primarily around perforations (Bruno 2001). Wang, Liu et al. (2015) identified that local buckling, connection failure and shear failure are the main failure modes in shale formation. However, the casing failure shape information are limited in C-W area, most of the deformation incidents were detected from mining shoe tripping in or bridge plug installation difficulties. The lead impression shape (as denoted in Figure 2.6) and multi-arm caliper well log image (like shown in Figure 2.7) both reveal the failure mode in C-W area matches the shear deformation type as illustrated in Figure 2.8.

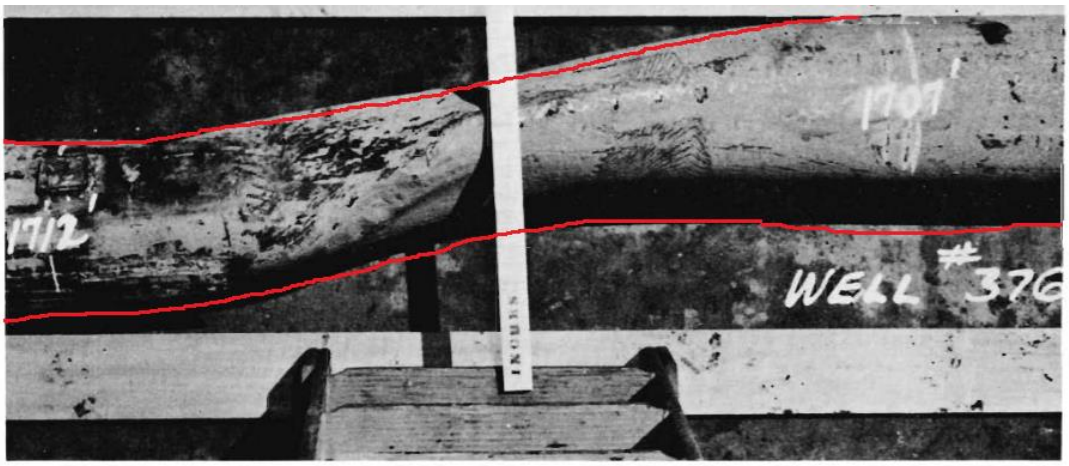


Figure 2.5 Earthquake induced overburden shear damage.
Source: Roberts (1953). This casing was measured between 1,707 and 1,712 ft.



Figure 2.6 Photo of lead impression in C-W area.
Source: CNPC.

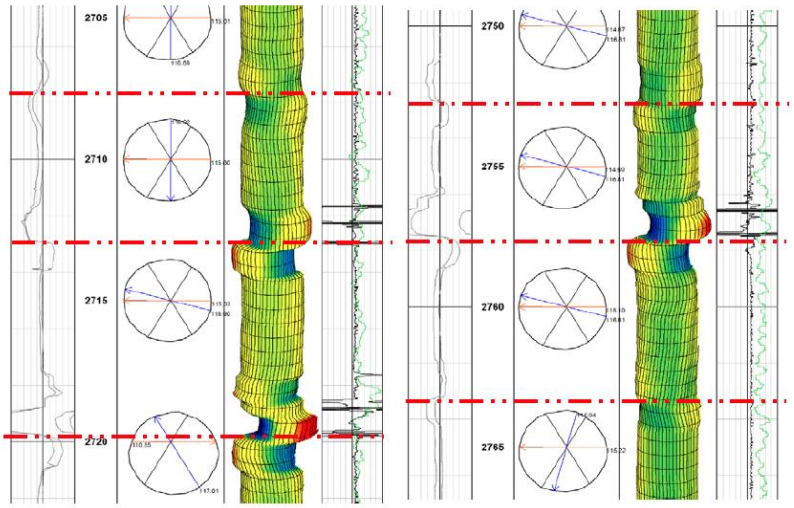


Figure 2.7 Multi-arm caliper well log image.
Source: CNPC.

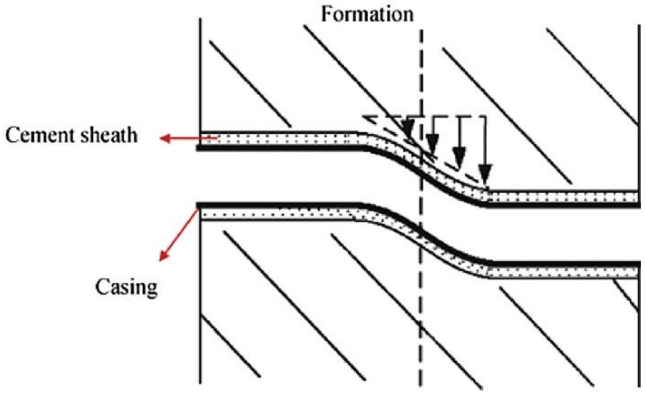


Figure 2.8 Schematic of casing shear deformation.
Source: Modified from Tian, Shi et al. (2015).

2.5 Possible Reasons of Casing Failure

Casing deformation is a compounded result of multiple contributing factors (as demonstrated in Figure 2.9). Lian, Yu et al. (2015) concluded that some casing failures were the joint result of rock property change, asymmetric treatment zones, and stress field redistribution using finite element modeling. Dusseault, Bruno et al. (2001) attributed the dominated casing-deformation mechanisms to localized horizontal shear at weak lithology interfaces and injection intervals. Daneshy (2005) concluded that casing failure is either caused by weak interfaces slippage or formation compaction. Tiejun, Hao et al. (2017) indicated that during fracturing process the rock mechanical strength change is a significant contributing factor of casing failure and improving casing ovality resistance is more effective than increasing steel grade.

In the production stage, the formation pressure decreases at pay zone due to oil and gas extraction. The production quantity varies by formation permeability and flow capacity. The stress difference between layers expands, and slippage will occur when the stress difference is above the shear stress limit between layer interfaces. The study of Yan, Ge et al. (2016) showed that fracturing not only generated tensile fractures, but can induce slip on pre-existing fractures. Maxwell, Urbancic et al. (2002) also pointed out that although the interaction between hydraulic fractures and pre-existing natural fractures contributes to the well production in extremely low permeability reservoirs, the fracture network complexity can also bring some concerns on casing deformation and well integrity.

Bao and Eaton (2016) concluded that fracturing operation pressurization can activate fault slippage. Chong, Li et al. (2017) pointed out that fault activation and

seismicity may cause underground water pollution as well as land subsidence. In Sichuan, China, according to Chen, Shi et al. (2017), 61.7% of the total deformation points are generated by faults/fractures or lithologic interfaces/bedding planes. From the outcrop and carvings observed in C-W area, the formation is well developed in beddings and weak planes. These two features illustrate that shale in this area has the potential of slip and break. Besides, from the micro-seismic data obtained during fracturing in Figure 2.10, a high intensity of micro-seismic signal was observed at the position of casing deformation areas. Since the high intensity micro-seismic signal is an indicator of the occurrence rock rupture or slip, the micro-seismic data provide a support that casing deformation in C-W area could be related to formation slippage. Among these multiple contribute factors, this research focus on the geological conditions that contribute to casing damage.

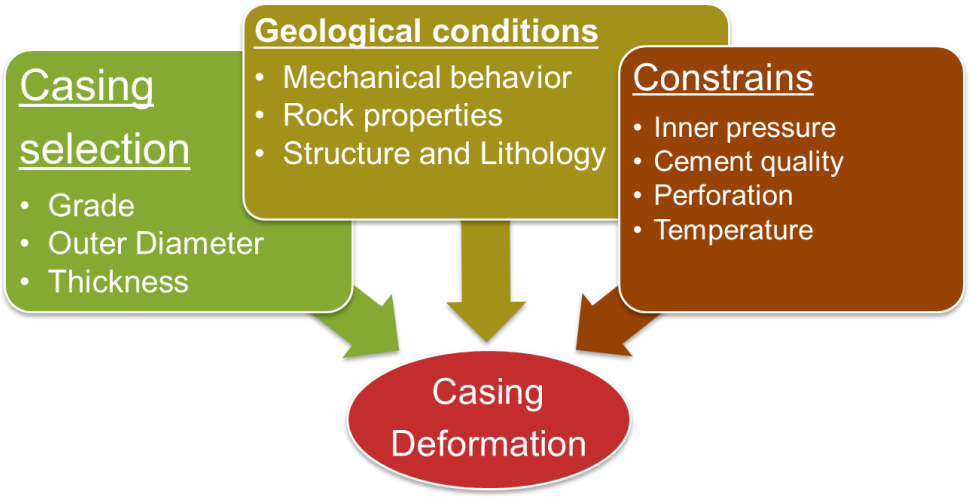


Figure 2.9 Possible reasons of casing deformation.

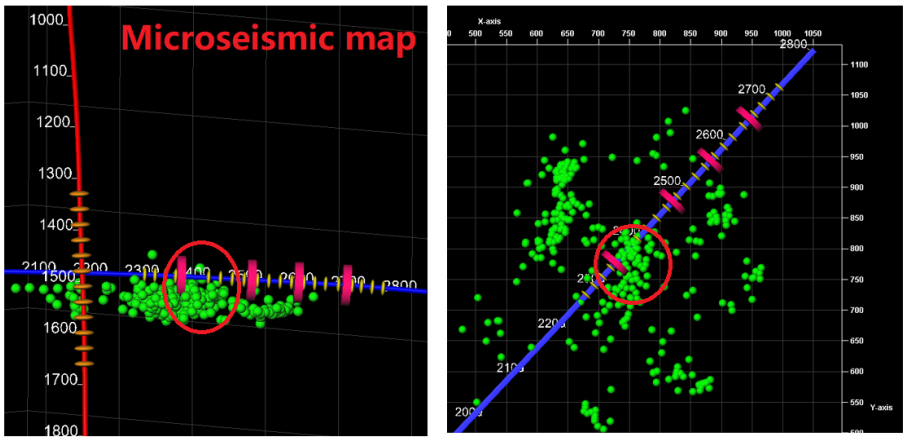


Figure 2.10 Micro-seismic map of a well in C-W area during fracturing. Source: CNPC. The red circle indicates the occurrence of high intensity signal at deform position.

Slip is the relative movement of geological bodies (fault, bedding, joint and others) on either or both sides of the interface. The slip criteria have many ways to describe, like yield criteria, fracture criteria, shear strength. In this research, Mohr Coulomb theory is taken for describing rock movement on weak lithology interface because of effective stress.

The shear resistance strength (frictional strength) between lithology contact surfaces have the relation as follows:

$$\tau = \mu\,(\sigma - p) \quad \text{.....(2.1)}$$

Where τ is the frictional strength, μ is the rock friction coefficient, σ is the rock stress, and p is the pore pressure.

If the frictional strength is smaller than the shear strength, there will not occur relative movement between the interface. (National Academies Press issuing and National Research Council . Committee on Induced Seismicity Potential in Energy Technologies 2013).

The linear Moore Coulomb's rule can be described as:

$$\tau_{max} = c' + \sigma_n' \tan \Phi' \text{.....(2.2)}$$

Where is τ_{max} the maximum shear stress before slippage, c' is the cohesion inside rock, σ_n' is the nominal effective stress of slippage plane, Φ' is the internal friction angle, c' and Φ' can be determined by experiment.

The heterogeneity of rock mechanical properties; the dip angle of the oil/gas layer; the mudstone expansion and creep after water absorption; salt rock creep, collapse and plastic flow; rock strata slide; fault activity; and sand production are all the possible geological reasons. The schematic of some of the possible geomechanically causes are demonstrated in Figure 2.11.

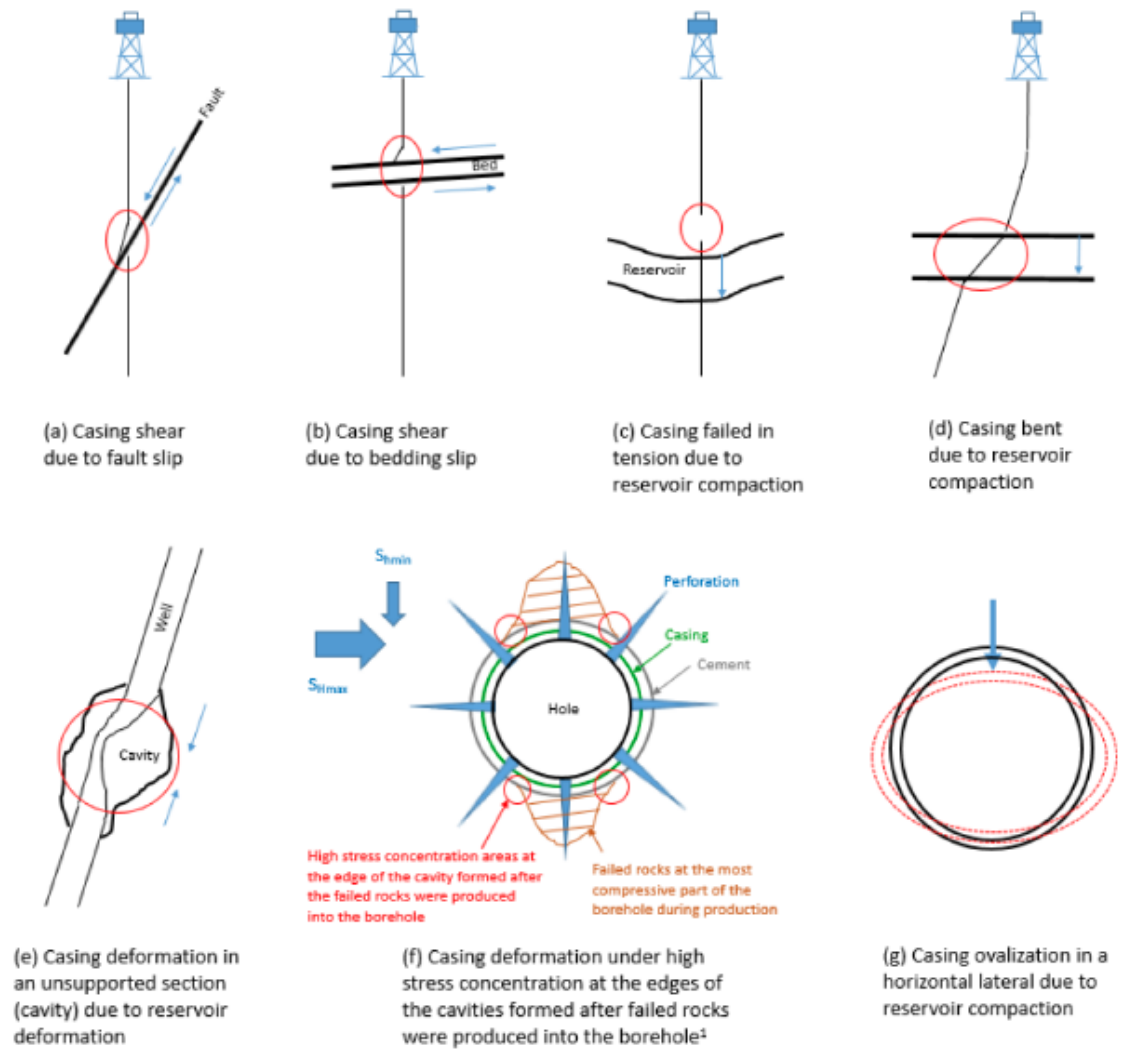


Figure 2.11 Schematic of possible geomechanics causes. Source: Tjengdrawira, Khaksar et al. (2017).

2.5.1 Connection with Lithology Discontinuities

The deformation points or damage location is the place where the change of casing size and shape affects the tools tripping in or out in the normal operation. The location of deformation point is represented by true vertical depth (TVD). Figure 2.12 shows the formation properties of a deformed X well in C-W area, the rock mechanical properties and stress distribution change significantly at and near the deformation point. When studying the TVD of 15 casing damage points in W area, an 86.7% of the damage points

are close to weak planes like natural fractures (NF), faults, beddings and lithology interfaces. As shown in Table 2.2, this correlation might reveal the mechanism of casing deformation. One hypothesis is that during hydraulic fracturing, hydraulic fractures (HF) get connected with lithology discontinuities and cause rock slippage. The redistribution of stress field applies extra stress on casing at some position. Due to this extra stress load, the chance of casing deformation at this parts increases.

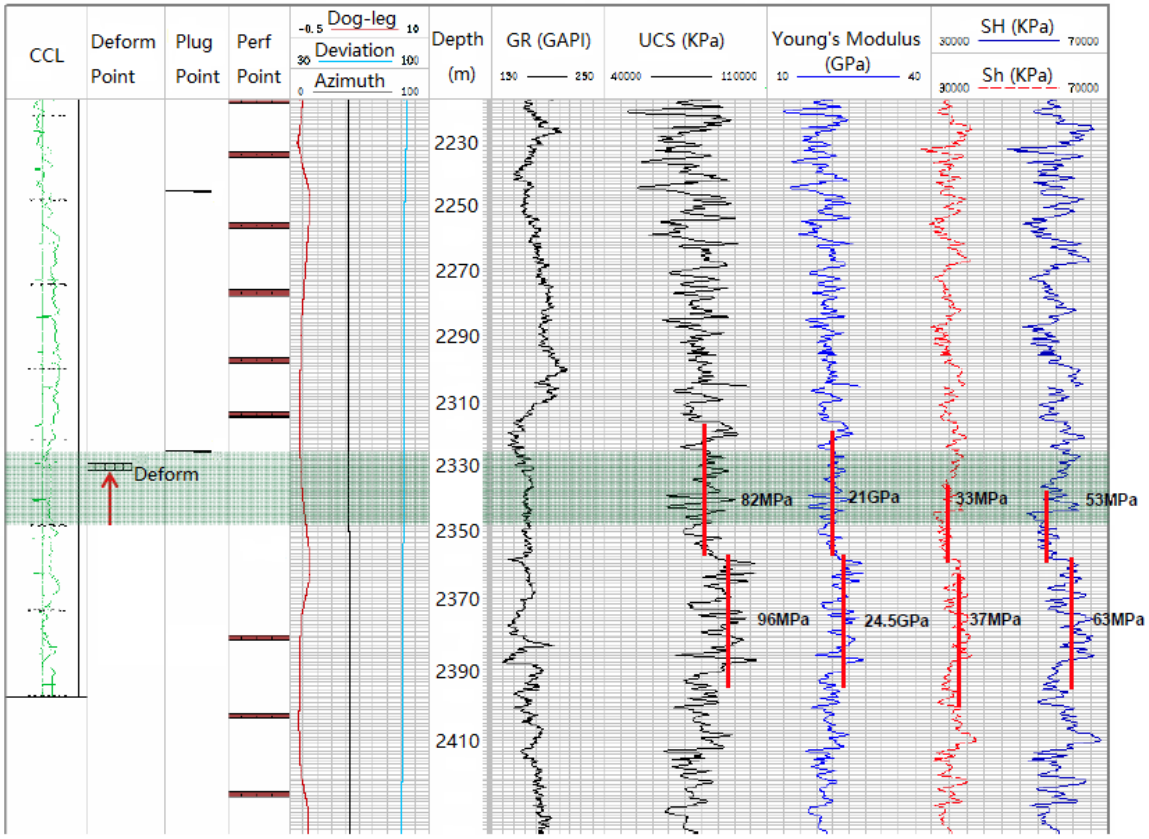


Figure 2.12 Well log data of X well in C-W area.
Source: CNPC. The deform point is indicated by the arrow. The Uniaxial Compressive Strength (UCS), Young's Modulus and horizontal stress values change dramatically near deform point.

Table 2.2 Lithology discontinuities observation at deform position.

Well NO.	TVD of Casing Damage Points (m)	If Close to Weak Planes
W202H1-1	2607	Yes
	2736	Yes
W202H1-2	2932	Yes
W202H1-6	3230	Yes
W202H3-1	3265	Yes
	3400	Yes
W202H3-2	3246	Yes
	3826	No
W202H3-3	2904	Yes
W202H3-4	3716	No
W202H3-5	2924	Yes
	3151	Yes
W202H3-6	3210	Yes
W204H4-2	5162	Yes
W204H5-3	4638	Yes

2.5.2 High Tectonic Stress and High Tectonic Stress Difference

The tectonic stress of several wells in C-W area are presented in Table 2.3. The average horizontal stress difference value is about 32% of the maximum horizontal stress and 47% of the minimum horizontal stress. The average ratio of the maximum horizontal stress and the minimum horizontal stress is 1.5. The relative magnitude of tectonic stress tensor plays an important role in unconventional play stability, especially during fracturing and production, when the stress field changes dramatically due to injection or extraction. Figure 2.13 illustrates the stress relation of three type of faults, where the three principal stresses, $\sigma_h, \sigma_H, \sigma_v$ are minimum horizontal stress, maximum horizontal stress, and vertical stress, respectively.

The direction and magnitude of tectonic stress determine the stress state of casing and is directly related to casing deformation. Compared with uniform tectonic stress field,

formation layer slippage and breakage have a higher occurrence risk under non-uniform tectonic stress. The large difference between the maximum horizontal stress and the minimum horizontal stress will increase the risk of slippage. The two typical stress types in this region are strike-slip and thrust (reverse) type. The movement of these two types are shown in Figure 2.14.

Table 2.3 Statistics of tectonic stress in C-W area.

Well NO.	TVD (m)	Maximum Horizontal Stress (MPa)	Minimum Horizontal Stress (MPa)	Vertical Stress (MPa)	Horizontal Stress Difference (MPa)	Tectonic Stress Mode	Horizontal Stress Difference /Max Horizontal Stress	Horizontal Stress Difference/ Min Horizontal Stress	Max Horizontal Stress/Min Horizontal Stress
N201-H1	2500	86	57.8	57	28	Thrust	33%	48%	1.5
NH3-1	2492	86	57.8	57	28.2	Thrust	33%	49%	1.5
N201	2500	86	57.8	57	28	Thrust	33%	48%	1.5
N206	1876	84	66	50	18	Thrust	21%	27%	1.3
W201-H1	1557	48	29	35	19	Strike-slip	40%	66%	1.7
W201-H3	2679	67	46	61	21	Strike-slip	31%	46%	1.5
Average	/	76.2	52.4	52.8	23.7	/	32%	47%	1.5

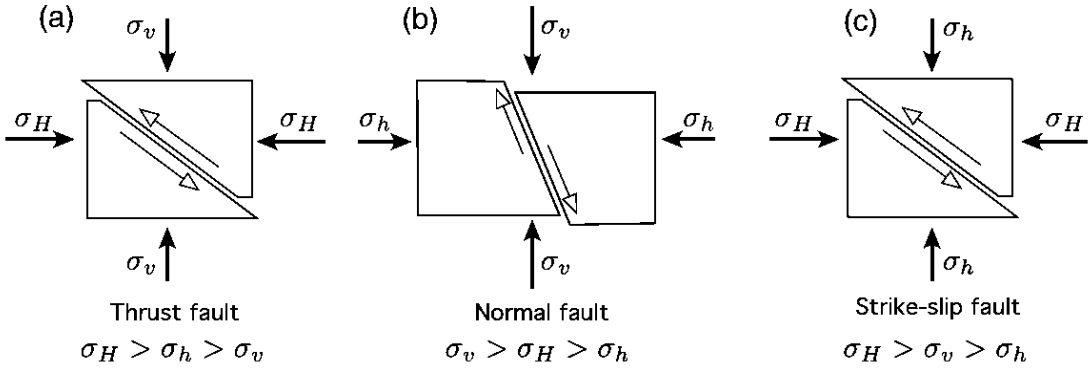


Figure 2.13 Three types of stress regimes.
(a) thrust fault, (b) normal fault, and (c) strike-slip fault.
Source: Council (2013). $\sigma_h\sigma_H\sigma_v$ represent minimum horizontal stress, maximum horizontal stress, and vertical stress separately. The relation between those three determine the stress regime and movement tendency.

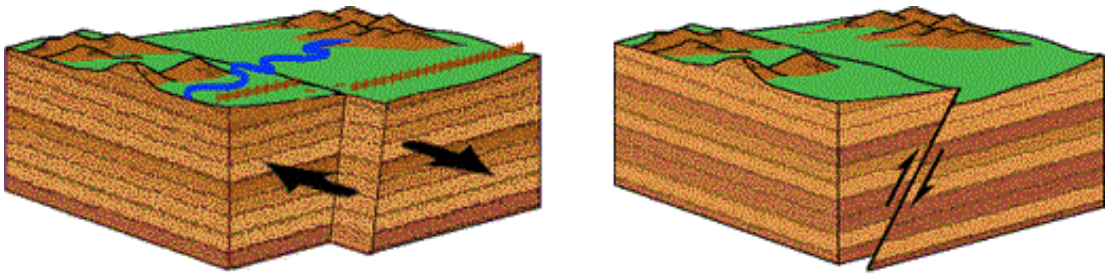


Figure 2.14 Diagram of strike-slip and thrust faults.
Strike-slip fault (left), thrust or reverse fault (right).
Source: Images from the U.S. Geological Survey Visual Glossary,
https://geomaps.wr.usgs.gov/parks/deform/gfaults.html .

Chapter 3: Methodology

The simulation software using in this research is Abaqus. In this chapter, the available fracture simulation methods in Abaqus will be introduced first. The computation method and cohesive zone method using in this model will be discussed by next. Finally, the process of how the simulation model was proposed and built up will be described in detail.

3.1 Introduction of Methods to Simulate Hydraulic Fracturing in Abaqus

There are four hydraulic fracturing simulation methods in Abaqus: (1) the Extended Finite Element Method (XFEM); (2) the Cohesive Seepage Element/Cohesive Zone Method (CZM); (3) the Concrete Damaged Plasticity Method (CDP); and (4) the simulation method based on remeshing. Their major functions and features are discussed separately as follows.

In XFEM, the propagation paths of fractures are not restricted by element boundary, so there is no need of remeshing after fracturing in this method, and the computation load is lower and easy to simulate. Besides, it can simulate tangential/gap flow (due to friction), fluid leak off or filtration, fracture reorientation in re-fracturing. The simulation of crossing fractures is not available in this method; however, it can be done through user defined functions.

In CZM, one or several cohesive elements with zero or closely to zero thickness are set up in advance to serve as the possible pathways of fracture propagation. Under this method, the tangential flow (friction) and the radial flow (filtration) can be modeled. One major advantage of this method is to simulate intersecting fractures in complex fracture network.

In CDP method, the tensile and compressive properties of rocks can be defined to describe the form of rock failure. However, the fluid flow pattern cannot be shown in this method.

For remeshing method, when the crack is extended once, the grid is remeshing once and the load is redefining once, then calculate the fracture parameters and predict the propagation direction, which can generate a large amount of computation load during this cycle.

Based on the features of the four common methods above, the method of XFEM and CZM can be used to simulate behaviors in hydraulic fracturing. In this research, the CZM is chosen to describe fractures in the simulation model.

3.2 Rock Elastic Constitutive Relation

In porous rock, the total stress can be expressed by Terzaghi's Principle (Terzaghi, Peck et al. 1996) as follows:

$$\boldsymbol{\sigma} = \boldsymbol{\sigma}' + \alpha\, p_w \qquad (3.1)$$

Where,

$\boldsymbol{\sigma}$ is the total stress, MPa;

$\boldsymbol{\sigma}'$ is the effective stress, MPa;

α is a porous medium constant independent of fluid properties, α=1 when it is full saturated, α is between 0 and 1 when un-fully saturated.

3.3 Fluid Flow in Cohesive Element

The fluid flow in normal and tangential directions in cohesive element is as presented in Figure 3.1.

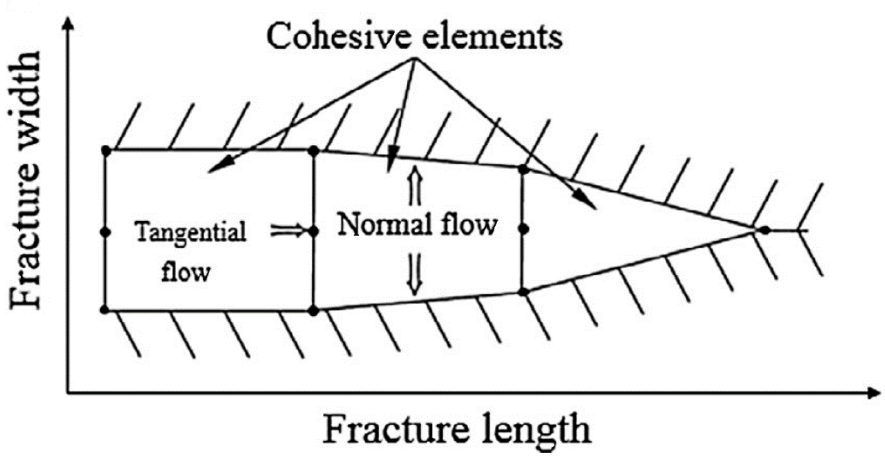


Figure 3.1 Flow within cohesive element.
Source: Guo, Luo et al. (2017). The fluid flow in a cohesive element is regarding to have two directions, the first it the tangential flow along the direction of the growth of fracture length, the second is the normal flow along the fracture width direction.

The two-typical fluid constitutive law in cohesive element are Newtonian and power law rheology. In this work, the fluid flow in fracture is assumed to be incompressible, single-phase, steady state Newtonian flow across the constant section area.

The governing equation of tangential flow is formulated as:

$$q = \frac{d^2}{12\mu} \nabla p \quad \text{.....(3.2)}$$

Where,

q is the volume flow rate in cohesive element, dimensionless;

d is the separation displacement of cohesive element, m;

μ is the viscosity of the fracturing fluid, mPa·s;

∇p is the fracturing fluid tangential pressure gradient, MPa/m.

The governing equation of normal flow is defined as:

$$\begin{cases} q_t = c_t\,(p_i - p_t) \\ q_b = c_b\,(p_i - p_b) \end{cases} \quad \text{.....(3.3)}$$

Where,

q_t is the normal volume flow rate into cohesive element upper surface, m^3/s;

q_b is the normal volume flow rate into cohesive element lower surface, m^3/s;

$c_t$is the fluid leak off coefficient on cohesive element upper surface, $m/s^{0.5}$;

c_b is the fluid leak off coefficient on cohesive element lower surface, $m/s^{0.5}$;

p_i-fluid pressure in the middle of the cohesive element, MPa;

p_t is the fluid pressure in the upper of the cohesive element, MPa;

p_b is the fluid pressure in the lower of the cohesive element, MPa.

3.4 Fluid-Solid Coupled Equilibrium Equation in Formation

The formation is assumed to be a solid skeleton porous media with single-phase, fully-saturated pores and the equilibrium condition of rock in any time. According to principle of virtual work, at any time t, the equilibrium equation can be given as:

$$\int_V (\boldsymbol{\sigma}' - P_P \boldsymbol{I}) \delta \boldsymbol{\varepsilon} dV = \int_S \boldsymbol{t} \cdot \delta \boldsymbol{v} dS + \int_V \boldsymbol{f} \cdot \delta \boldsymbol{v} dV \quad \text{.....(3.4)}$$

Where,

V is the control volume, m^3;

$\boldsymbol{\sigma}'$ is the effective stress, MPa;

P_P is the pore pressure, MPa;

$\boldsymbol{I}$ is the unit matrix, dimensionless;

$\delta \boldsymbol{\varepsilon}$ is the virtual strain rate, dimensionless;

S is the surface area under surface traction, m^2;

$\boldsymbol{t}$ is the surface traction vector, N;

$\delta \boldsymbol{v}$ is the virtual velocity vector, m/s;

$\boldsymbol{f}$ is the body force vector, N/m^3.

3.5 Fluid-Solid Coupled Continuity Equation in Formation

According to the law of conservation of mass, the fluid mass crossing the surface S at any time equals to the rate of the total fluid mass change in the control volume V to, and can be expressed as:

$$\frac{d}{dt}\left(\int_V \rho_f \, \varphi \, dV\right) + \int_S \rho_f \boldsymbol{n} \cdot \boldsymbol{v_{fp}} \, dS = 0 \quad \text{.....(3.5)}$$

Where,

ρ_f is the density of the pore fluid, kg/m^3;

φ is the porosity of the medium, dimensionless;

$\boldsymbol{v_{fp}}$ is the average velocity of the pore fluid relative to the solid phase, m^3/s;

$\boldsymbol{n}$ is the outward normal to surface S, dimensionless.

The pore fluid flow in the formation follows Darcy's law as:

$$\boldsymbol{v_{fp}} = -\frac{1}{\varphi g \rho_f} \boldsymbol{k} \cdot \left(\frac{\partial P_P}{\partial \boldsymbol{X}} - \rho_f \boldsymbol{g}\right) \quad \text{.....(3.6)}$$

Where,

$\boldsymbol{g}$ is the gravity acceleration vector, dimensionless;

g is the magnitude of gravity acceleration, m/s^2;

$\boldsymbol{k}$ is the hydraulic conductivity of the porous medium, m/s;

P_P is pore pressure, MPa;

$\boldsymbol{X}$ is a spatial coordinate vector, dimensionless.

The effective mechanical response of the solid skeleton can be described with either elastic or elastic-plastic constitutive models. The plastic behavior follows the Drucker-Prager model (Drucker and Prager 1952), which is generally used to represent the constitutive behavior of granular and geological materials. The yield criterion for

Drucker-Prager model is based on the shape of the yield surface in the meridional plane. The yield surface has a linear form, and can be expressed as:

$$F = q' - p' tan\beta - d = 0 \quad \text{.....(3.7)}$$

Where,

F is the yield function;

p' is the effective mean stress, defined by the effective stress tensor $\boldsymbol{\sigma}'$ as:

$p' = -\frac{1}{3}\, trace(\boldsymbol{\sigma}')$, MPa;

q' is the deviatoric stress, defined by the effective deviatoric stress tensor **s** as:

$q' = \sqrt{\frac{3}{2} s : s}$;

β and d are the friction angle and cohesion of the material in $q' \sim p'$ plane, respectively.

3.6 Cohesive Zone Method (CZM)

Dugdale (1960) and Barenblatt (1962) first introduced the concept of Cohesive Zone Method (CZM). CZM is a method to study fracture failure, it considers the nonlinear relation at fracture tip and has an advantage in describing the plastic zone and softening effects at fracture tip in shale (Haddad and Sepehrnoori 2015). Meanwhile, it can also study the fracture initiation and propagation under different loads. The core concept of CZM is using the relation of local stress-displacement to describe fracture behavior.

In this study, CZM is used in setting up the simulation model. According to Systèmes (2014), the cohesive model defined by traction-separation law assumes an initial linear elastic relation before damage and element failure is defined by material stiffness degradation.

In Abaqus, before the damage of cohesive element, the constitutive relation of CZM is linear elasticity. Elastic behavior is described by an elastic constitutive matrix with nominal stresses and nominal strains across the interface as described in

$$\boldsymbol{t} = \begin{Bmatrix} t_n \\ t_s \\ t_t \end{Bmatrix} = \begin{bmatrix} K_{nn} & K_{ns} & K_{nt} \\ K_{ns} & K_{ss} & K_{st} \\ K_{nt} & K_{st} & K_{tt} \end{bmatrix} \begin{Bmatrix} \varepsilon_n \\ \varepsilon_s \\ \varepsilon_t \end{Bmatrix} = \boldsymbol{K}\varepsilon \quad \text{.....(3.8)}$$

Where,

t is the cohesive element traction stress vector, dimensionless;

t_n is the normal stress, MPa;

t_s, t_t are the first shear stress and second shear stress, MPa;

K_{nn} is the Young's modulus, MPa;

K_{ss} K_{tt} are the shear modulus, MPa;

$\varepsilon_n, \varepsilon_s, \varepsilon_t$ are the dimensionless strains in normal, first shear, and second shear directions, dimensionless; and ε_n, ε_s, ε_t are defined as:

$$\varepsilon_n = \frac{d_n}{T_o}, \varepsilon_s = \frac{d_s}{T_o}, \varepsilon_t = \frac{d_t}{T_o} \quad \text{.....(3.9)}$$

Where d_n, d_s, d_t are the displacements in normal, first shear direction, and second shear direction. T_o is the cohesive element thickness. For 2D simulation, the component of second shear direction does not exist.

The damage of cohesive element in Abaqus follows the traction-separation mode, which demonstrates the relation between interface interaction and interface separation displacement as shown in Figure 3.2.

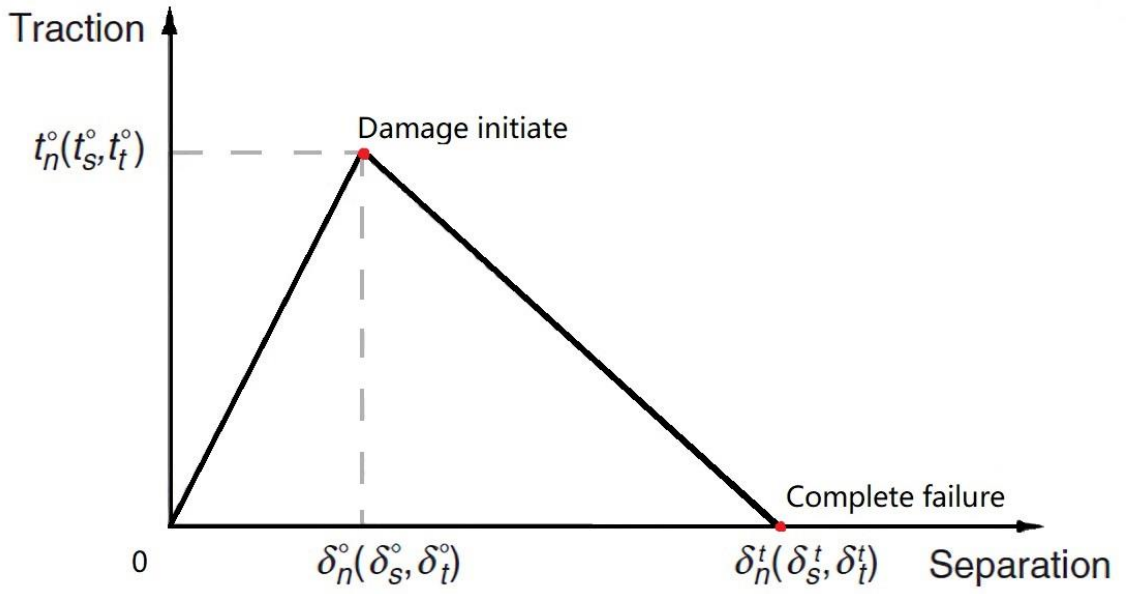


Figure 3.2 Cohesive traction-separation constitutive relation.
When the cohesive element separation is between 0 to $\boldsymbol{\delta^0_{n,s,t}}$, the relation between separation and traction is a linear elastic relation, once the separation reaches $\boldsymbol{\delta^0_{n,s,t}}$, damage initiates, the time $\boldsymbol{t^0_{n,s,t}}$ at this point is the damage initiation time. Once the separation gets to $\boldsymbol{\delta^t_{n,s,t}}$, cohesive element completely fails.

3.7 Cohesive Element Initiation

Elastic relation section is the part before damage initiates, where $\delta < \delta^0$. The relation between traction and separation is linear. There are several damage initiation criteria offered by Abaqus to choose. And in this model we take the damage initiation type as quadratic nominal stress criterion, which means that damage initiates in a quadratic interaction function, and the quadratic nominal stress criterion relation is described as (Systèmes 2014):

$$\left\{\frac{\langle t_n \rangle}{t_n^0}\right\}^2 + \left\{\frac{t_s}{t_s^0}\right\}^2 + \left\{\frac{t_t}{t_t^0}\right\}^2 = 1.. \quad \text{.....(3.10)}$$

Where,

t_n^0, t_s^0, t_t^0 represent the damage imitation peak values for nominal, first and second shear direction, respectively. The symbol < > here is the Macaulay bracket, its mathematical definition is $\langle t \rangle = \frac{|t|+t}{2}$. Damage is assumed to initiate when a quadratic interaction function involving the nominal stress ratios (as defined in the expression below) reaches a value of one.

The quadratic nominal strain criterion can be represented as:

$$\left\{\frac{\langle \varepsilon_n \rangle}{\varepsilon_n^0}\right\}^2 + \left\{\frac{\varepsilon_s}{\varepsilon_s^0}\right\}^2 + \left\{\frac{\varepsilon_t}{\varepsilon_t^0}\right\}^2 = 1 \quad \text{.....(3.11)}$$

When the sum of stress ratio gets to 1, damage initiates.

3.8 Cohesive Element Propagation

Softening part is the process of damage evolution, where $\delta^0 < \delta < \delta^f$. when the stress applying on cohesive element reaches to its ultimate tensile strength, damage occurs. The maximum stress it can resist decreases with the increasing of separation displacement until 0, when the cohesive element it totally damaged.

There are two types of damage evolution types of cohesive element: one is based on effective displacement, the other is based on energy dissipation principle.

(1) Damage evolution based on effective displacement

When damage initiate, the element stiffness declines. The damage at interface is used a dimensionless coefficient to demonstrate. It's ranging from 0 to 1, when no damage occurs, D=0, when damage completes, D=1. The stress under the influence of damage coefficient D is expressed as:

$$t_n = \begin{cases} (1 - \mathrm{D})\ \bar{t_n}, & \bar{t_n} \geq 0 \\ \bar{t_n}, & \bar{t_n} < 0 \end{cases} \quad \text{.....(3.12)}$$

$$t_s = (1 - \mathrm{D})\ \bar{t_s} \quad \text{.....(3.13)}$$

$$t_t = (1 - \mathrm{D})\,\bar{t_t} \quad \text{.....(3.14)}$$

Where $\bar{t_n}, \bar{t_s}, \bar{t_t}$ are the stress components read from the elastic traction-separation relation curve without damage. The damage coefficient D here is:

$$\mathrm{D} = \frac{\delta_m^f(\delta_m - \delta_m^0)}{\delta_m(\delta_m^f - \delta_m^0)} \quad \text{.....(3.15)}$$

Where,

δ_m^0 is the effective displacement at damage initiation, m;

δ_m^f is the effective displacement at damage completion, m;

δ_m is the effective displacement during loading, m;

$\delta_m = \sqrt{\langle\delta_n\rangle^2 + {\delta_s}^2 + {\delta_t}^2}$ (Camanho and Dávila 2002).

(2) Damage evolution based on energy dissipation principle

The energy here represents the breaking energy during fracture extension. The numerical value equals to the area under the traction-separation curve. The behavior selected in this model is a mix mode behavior of Power Law form and Benzeggagh-Kenane (BK) form.

The Benzeggagh-Kenane fracture proposed by Benzeggagh and Kenane (1996) can be given by:

$$G_n^C + (G_s^C - G_n^C)\left\{\frac{G_S}{G_T}\right\} = G^C \quad \text{.....(3.16)}$$

Where $G_S = G_s + G_t$, $G_T = G_n + G_S$, G_n.

G_s and G_t represents the work done by stress in nominal, first shear and second shear direction. G_n^C, G_s^C, G_t^C are the critical fracture energy in each direction.

The Power Law form is given by:

$$\left\{\frac{G_n}{G_n^C}\right\}^{\alpha} + \left\{\frac{G_s}{G_s^C}\right\}^{\alpha} + \left\{\frac{G_t}{G_t^C}\right\}^{\alpha} = 1 \quad \text{(3.17)}$$

Where α describes the correlation between evolution forms.

Delaminating part: $\delta > \delta^f$, no more traction between two paces.

3.9 Model Constructions

During hydraulic fracturing, the induced hydraulic fracture can connect with natural fractures and cause slippage on weak planes. Besides, shale is water-sensitive, shale formation can swell and creep during fracturing because of the injecting fluid, which can also lead to formation slip.

Chipperfield, Wong et al. (2007) built a mechanical model to illustrate the casing deformation induced by formation shear expansion effect. Furui, Fuh et al. (2010) studied the declination of rock mechanical properties in acidizing fracturing, which will lead to the instability of wellbore and cause displacement in axial direction. To reveal the response of casing deformation under rock slip, Yin, Han et al. (2018) built a 4 m×12 m, 3D FEM model containing casing, cement in slip rock like presented in Figure 3.3 to simulate slippage displacement.

Different slip displacement values are input into this three-dimensional FEM of casing to predict the casing stress and deformation. The relation of axial position (horizontal position on wellbore) and the Von Mises applying on casing is as shown in Figure 3.4. The slip displacement being simulated contain 4 mm, 8 mm, 12 mm, 16 mm and 20 mm.

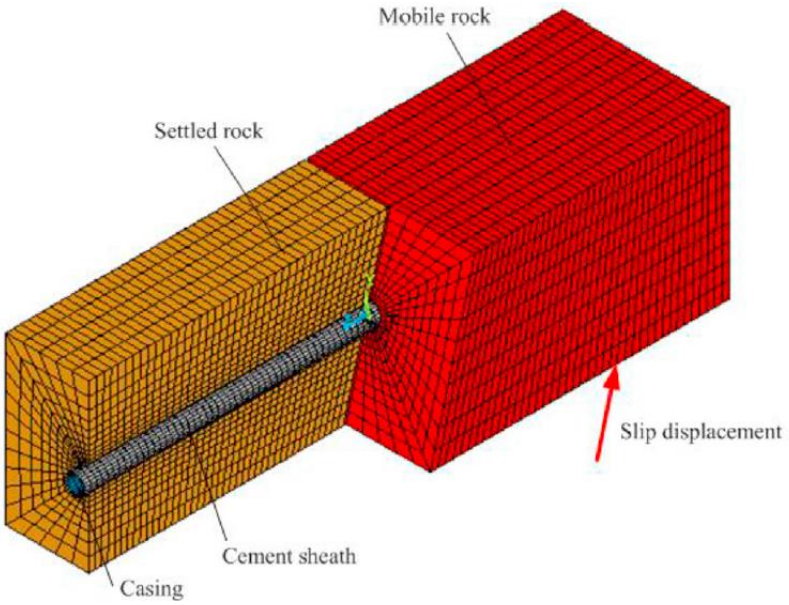


Figure 3.3 Schematic model of 3D finite element model of casing in slip rock. Source: Yin, Han et al. (2018). The yellow block is a fixed settled block, while the red block is a mobile rock that can move along the interface of these two blocks and create slip displacement. A casing with cement sheath locates in these two blocks. The slip displacement will apply stress on casing.

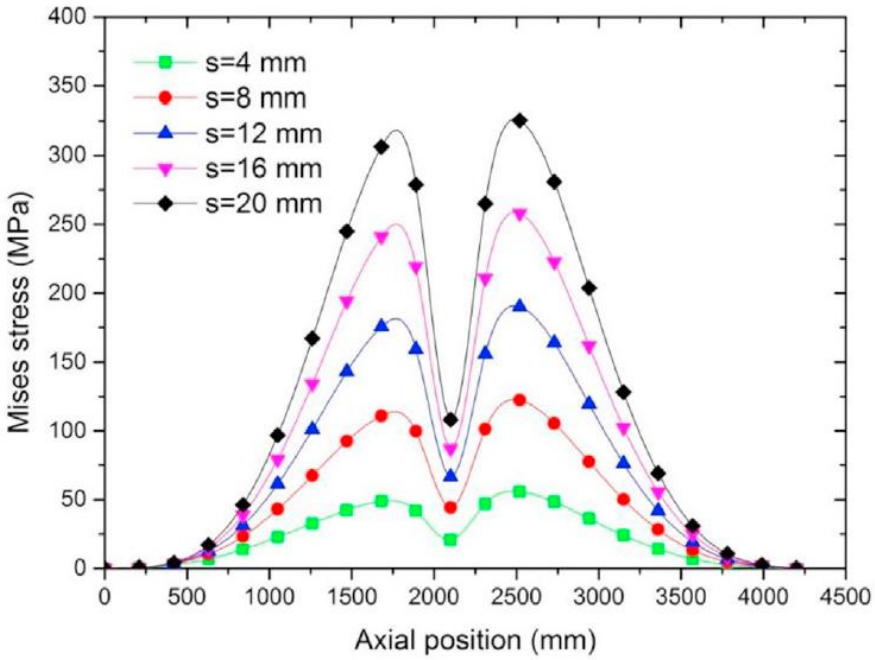


Figure 3.4 Casing Von Mises stress distribution under various slip displacements. Source: Yin, Han et al. (2018). The slip displacement value between settled rock and mobile is set from 4 mm, 8 mm, 12 mm, 16 mm, to 20 mm. as the displacement increases, the Mises stress applying on casing increases. And the stress regime is symmetrical with the rock slip face.

To investigate the response of casing and formation during fluid injection, a system containing casing and slip plane is required in the model. The target problem in complex fracture network is illustrated in Figure 3.5. To simplify the system and be more specific on the mechanism of response of fractures during fracture, only one hydraulic fracture (HF) and one intersecting natural fracture (NF) are selected to study their behavior during injection. The natural fracture (NF) in this research represents any weak geological discontinuities like natural fractures, faults, beddings and other lithology interfaces. Besides, due to the complication of stimulated fracture system. Only one HF and one NF are selected to study neglecting the fracture shadowing effect. Figure 3.6 shows a diagram of the three-dimensional position of intersecting HF and NF. To obtain a high computational efficiency, this 3D model is further simplified by assuming 2D KGD fracture model (Zheltov, 1955; Geertsma and De Klerk, 1969) as illustrated in Figure 3.7. The schematic diagram for the simplified 2D model is as illustrates in Figure 3.8.

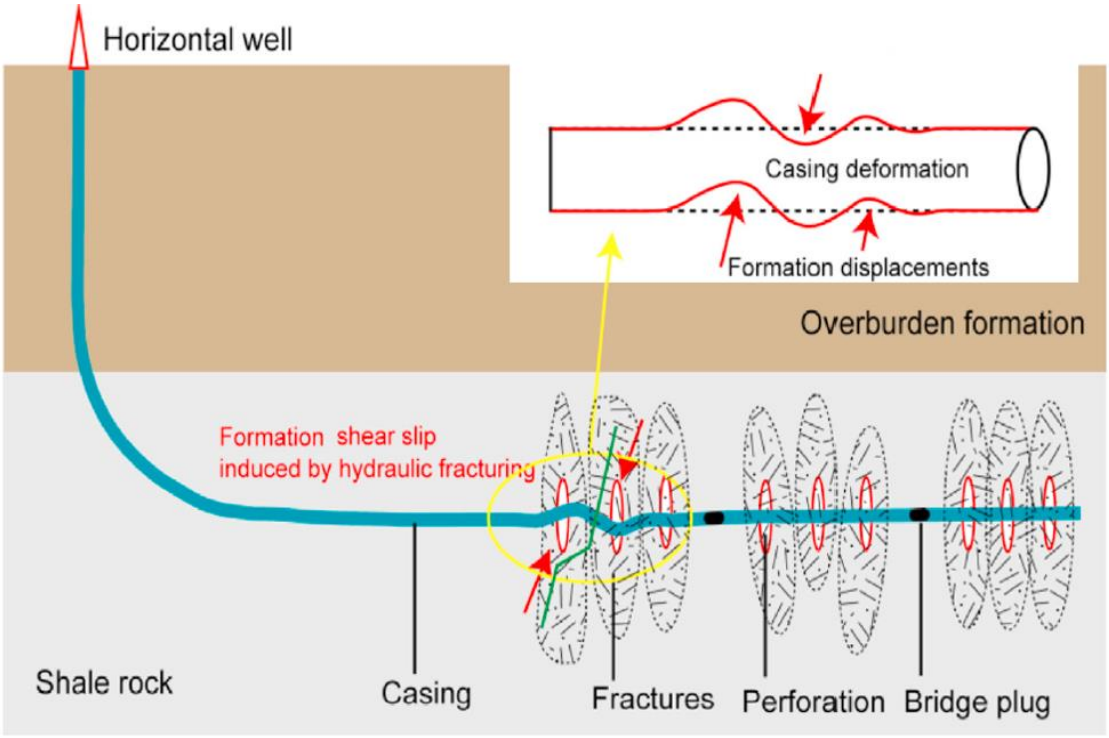


Figure 3.5 Schematic diagram of natural fracture slip induced slip.
Source: Yin, Han et al. (2018). In the fracture system consist of hydraulic fractures and natural fractures, the formation swells, or triggered formation slip can cause casing S shape deformation.

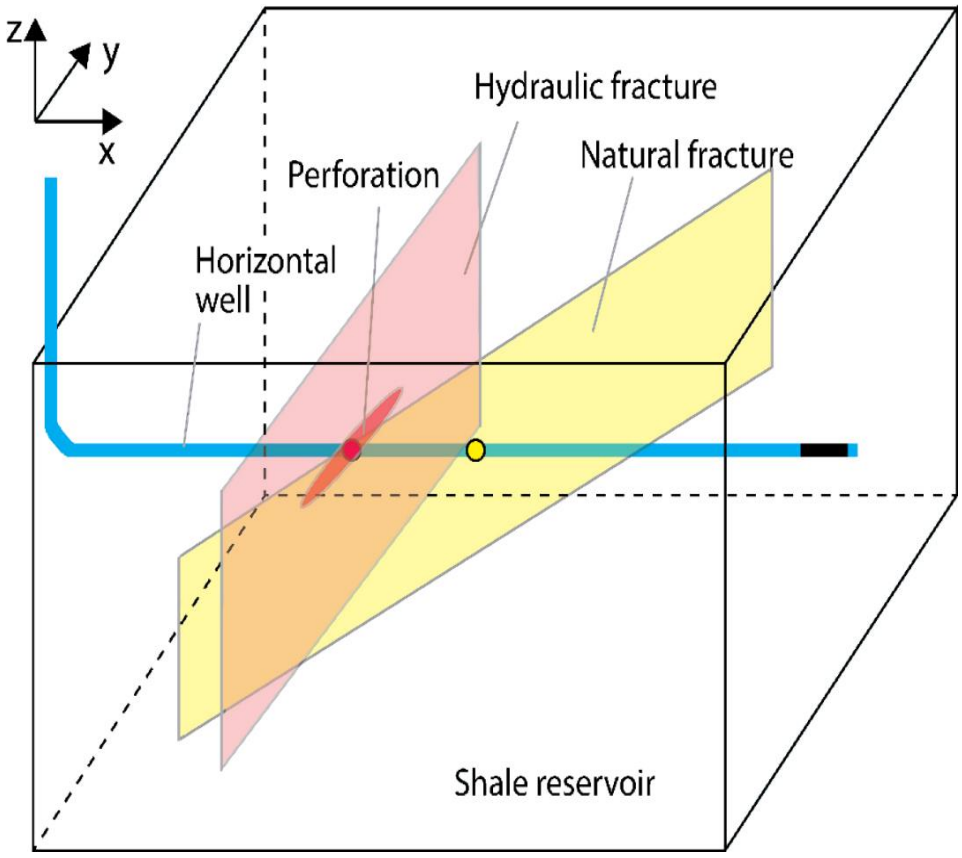


Figure 3.6 3D schematic of fractures and wellbore.
The blue line represents the horizontal well, the light red plane denotes hydraulic fracture, while the yellow plane illustrates natural fracture. Perforation and injection point are plotted in dark red.

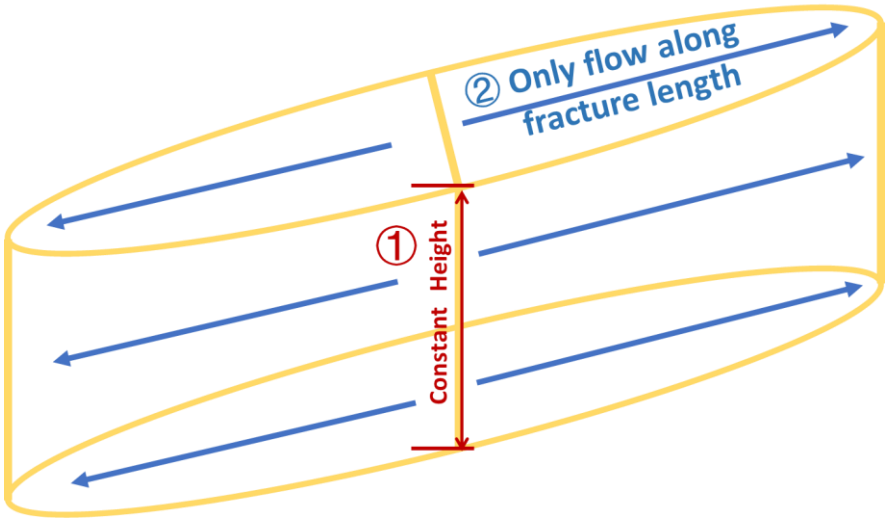


Figure 3.7 Fracture model assumption.
Taking the assumption of THE classic 2D KGD Model that the fracture height is constant and there is only flow along the fracture length direction.

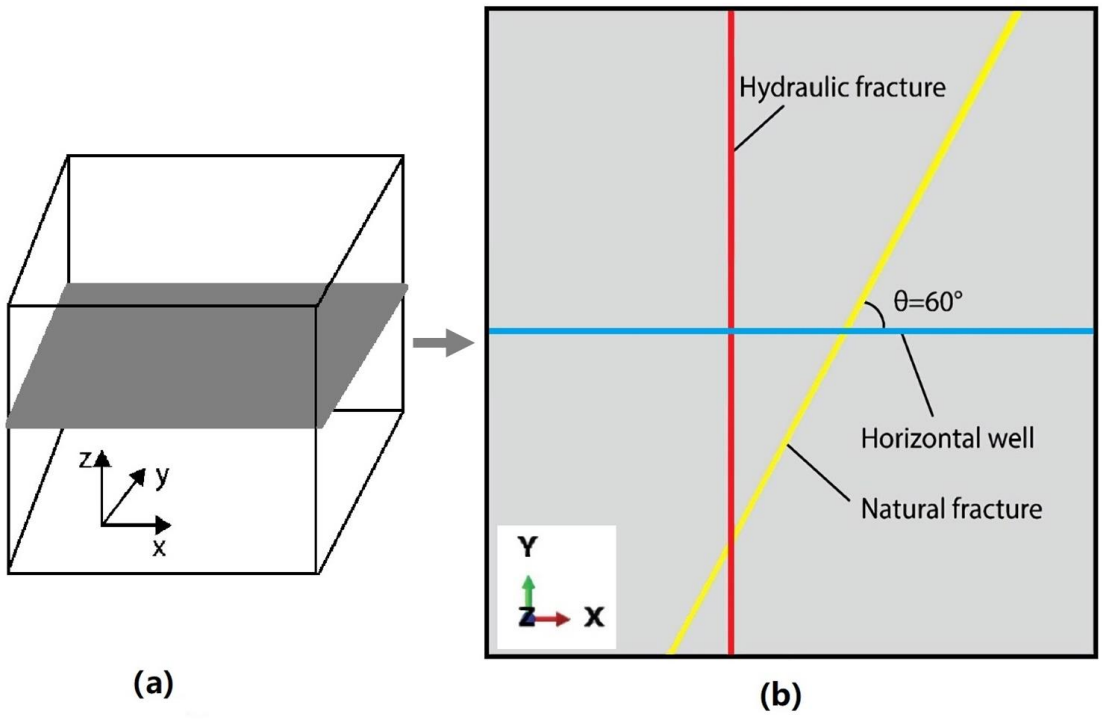


Figure 3.8 Schematic of simplification from 3D model to 2D model.
The graph on the right represents the horizontal plane took from the formation cubic on the right. The blue line is used to represent horizontal wellbore, red solid line equals to the HF while NF is denoted by the solid yellow line. The intersecting angle between HF and NF is 60 degrees.

3.10 Model Assumptions

In setting up the model, all perforation stages in the horizontal segment of the well are assumed to be evenly spaced and symmetric with the cluster center. Formation properties in the drainage area is represented by a segment between two stages. Therefore, in this study, only one perforation cluster is selected and studied in detail to represent all stages. The ballooning effect of casing and cement sheath is further neglected. By neglecting the voids between interfaces and within cements, the shear stress applying on casing equals to the one applying on wellbore. Therefore, it is safe to assume that the cement sheath and casing can be neglected and represented by wellbore in this model.

In summary, to simplify the complicate mechanisms during fracturing, additional assumptions are made as follows:

(1) The formation is single layer with homogeneous, isotropic and continuous properties;

(2) The formation stress-strain has a linear elastic relation;

(3) Created hydraulic fracture is modeled by planar bi-wing shape (ideal fracture) with a constant height;

(4) Fracturing fluid is incompressible and fully saturated the pores following the Newtonian laminar flow;

(5) No chemical reaction between fracturing fluid and rock;

(6) Fluid leak-off coefficient is a constant;

(7) No stress shadowing effects between fractures;

(8) The influence of temperature field is neglected;

(9) The response of cement sheath and casing is represented by the deformation along horizontal wellbore location.

3.11 Model Set-up

To account of the characters of the porosity rock media, a coupled poro-elastic finite element model (FEM) is used. The dimension of the model is defined as 100 m×100 m in a square plane shape. The intersection angle between the HF and NF is 60°, while the HF and NF are embedded in the formation with cohesive elements. The intact rock is meshed with the FSC (flow-solid coupling) element: CPE4P (4-node bilinear displacement and pore pressure), and the HF and NF are meshed with pore-pressure cohesive element: COH2D4P (4-node two-dimensional pore pressure cohesive element)

as demonstrated in Figure 3.9. The modeling theories taken in building model are the relation before HF-NF intersection, the deformation type of NF is elastic deformation, and after stress exceeding yield strength, NF will lose efficacy and fail. The boundaries in both x and y directions are fixed boundaries, which means that the model cannot move in either x direction or y direction Through this 2D HF-NF model the mechanism of NF extension can be performed and studied. To build up a model, the process contains: (1) defining and partition model geometry in part, fabricate hydraulic fracture (HF) and natural fracture (NF) in model; (2) describing material properties; (3) assembling parts; (4) mesh assembly parts with quad-element, define cohesive element in mesh for HF/NF, and merge injection node in mesh; (5) deciding analysis steps and output fields; (6) specifying load and boundary conditions. The dimension details are denoted in Figure 3.10.

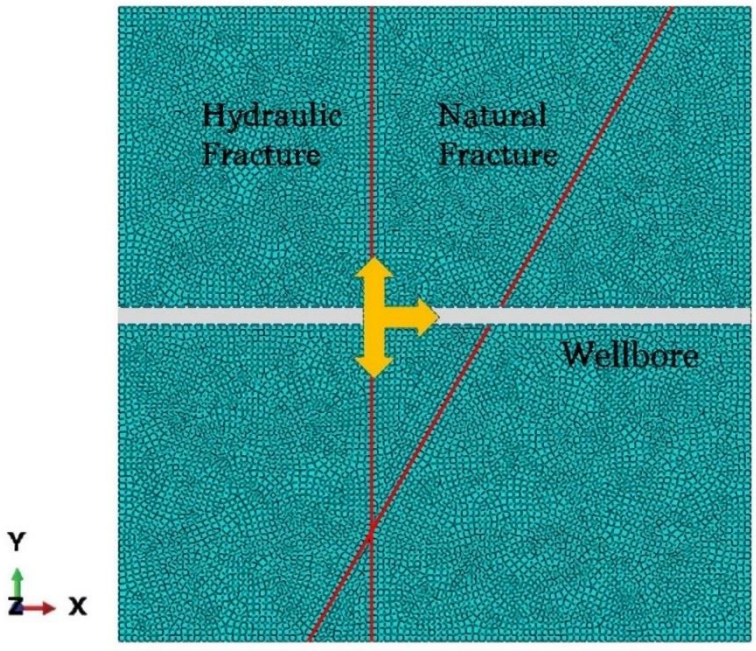


Figure 3.9 Finite element model with mesh.
The yellow arrow represents the injecting fluid flow direction from injection point, HF and NF are both denoted in red.

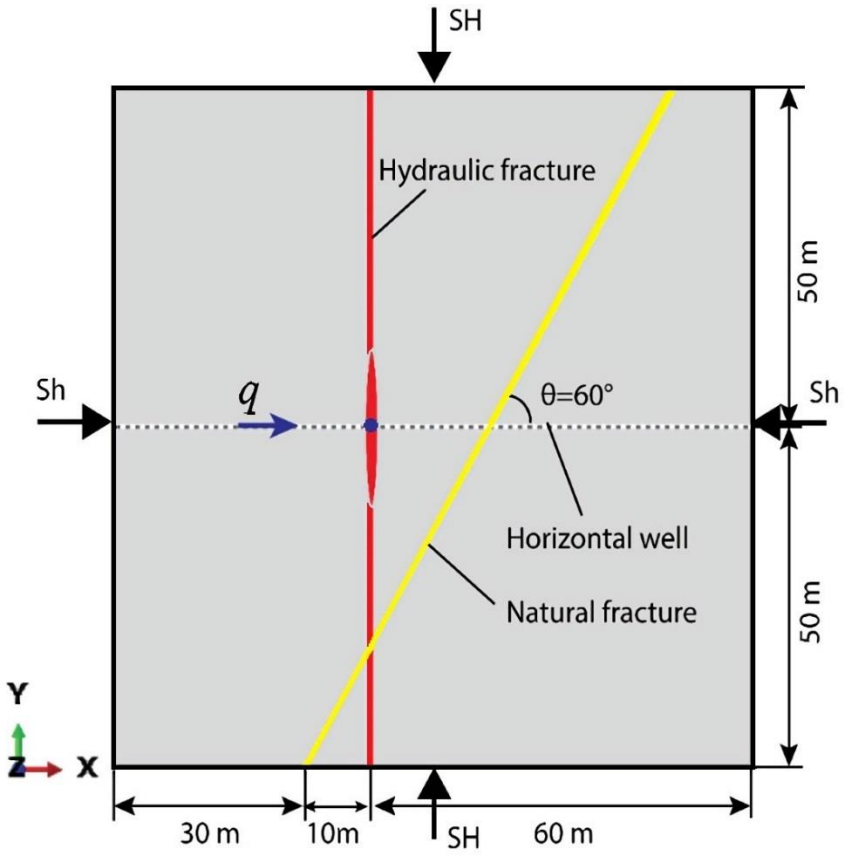


Figure 3.10 2D model of fractures and wellbore.
The dashed line is used to represent horizontal wellbore, red solid line equals to the HF while NF is denoted by the solid yellow line. The intersecting angle between HF and NF is 60 degrees. The size of this model is 100 m×100 m.

Chapter 4: Case Study

4.1 Case Study Well Information

In C-W area, the porosity of the shale reservoir is in the range of 2~18%, and the gas permeability lies between 0.005~0.1 mD. There is no direct log data can prove the existence of casing deformation or the shape and size of deformation location. The casing deformation is detected though encountering difficulty when setting the third bridge. The deformation points of the studying well W2X is at TVD of 2331.5 m.

4.2 Case Study Input

The simulation is performed based on the features of W2X shale gas plays. The input parameters are listed in Table 4.1.

Table 4.1 Input parameter for 2D base model simulation

Parameter	Value	Unit
Young's modulus	21	GPa
Poisson's ratio	0.25	-
Tensile strength	2.9 (HF), 1.45 (NF)	MPa
Shear strength	20 (HF), 12 (NF)	MPa
Matrix permeability	0.1	mD
Void ratio	0.02	-
Critical fracture energy	30	J/m^2
Leak-off coefficient	2×10^{-12}	$m^2/s/Pa$
Fluid viscosity	1	mPa·s
Maximum horizontal stress S_H	53	MPa
Minimum horizontal stress S_h	33	MPa
Vertical stress S_v	48	MPa
Initial pore pressure	23	MPa
Injection rate	0.0003	m^2/s
Specific weight of fluid	9800	N/m^3

4.3 Case Study Results

Fracture Propagation

The initiation and propagation of HF and NF are shown in Figure 4.1. To observe the change more obvious and direct, the deformation value is exaggerated 100 times in x-direction, and 10 times in y-direction. The PFOPEN output here represents the pore fracture opening at integration outputs.

Figure 4.1 (a) and (b) shows that, as injection keep going, the length of HF extends. The hydraulic fracture width gets the maximum value at wellbore and decreases as moving away from wellbore, the width distribution of HF is in an ellipse shape. After 450 s, HF gradually gets close to NF and eventually intersects at 451.7 s. Once HF-NF intersection occurs, HF stops propagating and is being diverted into the pre-existing NF at the intersection point while injecting fluid continues to flow into the pathway of NF. This procedure happens within one second, and the detailed process of intersection are demonstrated in Figure 4.1 (c) and (d). These two graphs occurring at the same time point of 451.7 s, but with different calculation step. What's more, after intersection, as presented in Figure 4.1 (e) and (f), due to the shunting action of injecting fluid, the open width of HF decreases.

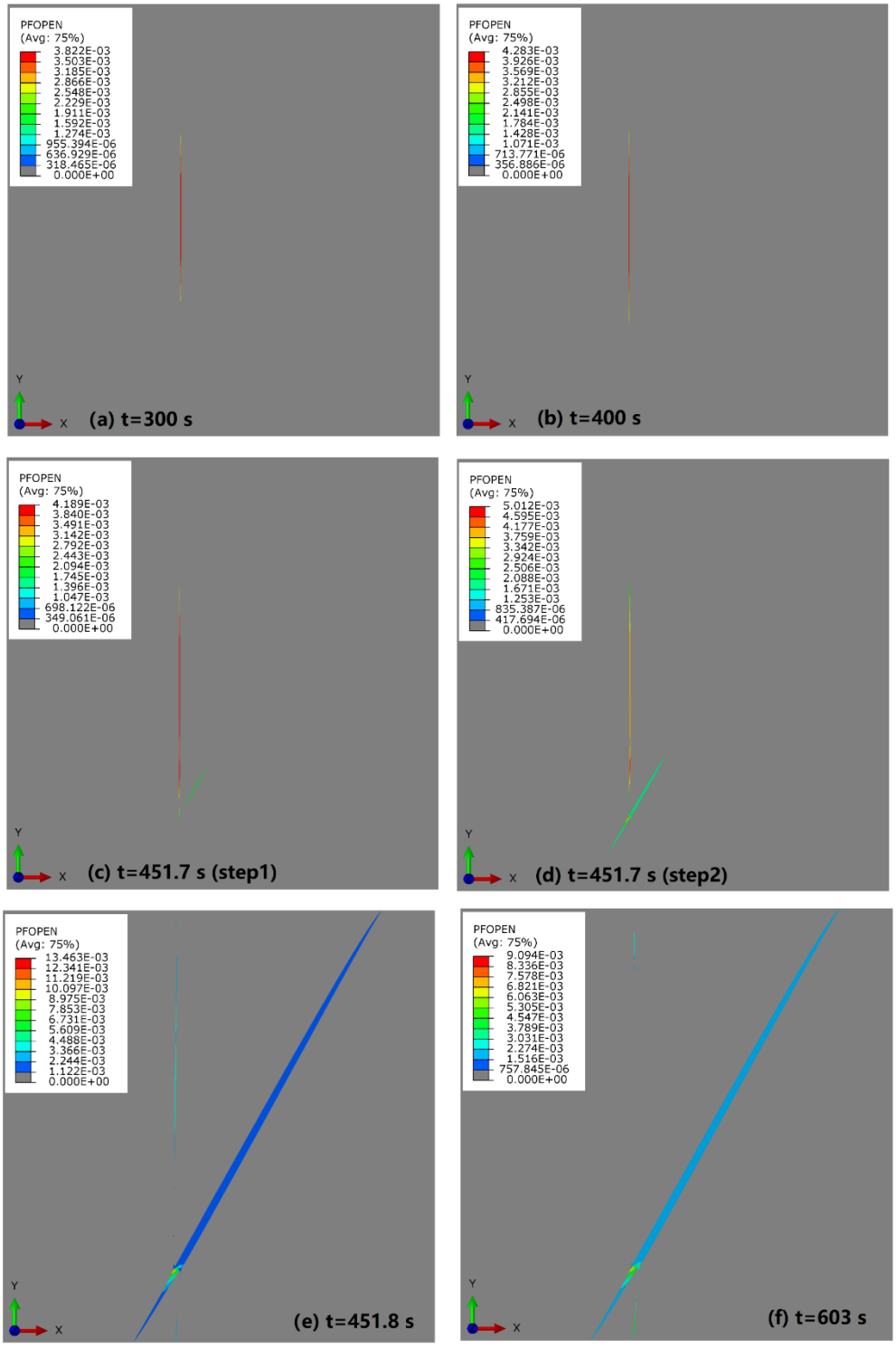


Figure 4.1 Fracture propagation trace at different time.
HF and NF intersect at 451.7 s. Before intersection, like presented in (a) and (b), HF propagates with time. Once intersection occurs, besides flowing in HF, fracturing fluid also gets into NF and pass rapidly in a short time. (c) and (d) all occurred at 451.7 s, but different time step. (e) and (f) represent the change after intersection.

Rock Deformation and Slippage

The four cloud graphs in Figure 4.2 illustrate the displacements in the y-direction before intersecting the natural fracture. The injecting time are at 55 s, 105 s, 205 s, and 300 s separately. The y-direction displacement is denoted by the symbol U2, while the unit of U2 is in meters. As time goes, y-direction displacement value increases and the area with higher displacement value range expands. The y-direction displacement value is symmetrical with the horizontal well in opposite directions.

HF and NF intersect at 415.7 s, and the intersection process is as demonstrated in Figure 4.3. The y-direction displacement first becomes asymmetry, then the degree of asymmetry expands with time. And finally, an asymmetry y-direction displacement occurs along the NF, which indicates the occurrence of relative movement. The relative movement continues to rise with time.

For the y-direction displacement distribution, taking the cloud graph of 603 s like shown in Figure 4.4 as a representative, the displacement is not symmetrically distributed with horizontal well. Besides, as demonstrated in Figure 4.5, there is an opposite slippage on the two sides of NF, the formation on the left of NF has a tendency of slippage downwards, while the formation on the right side tends to move upwards. This deformation change form symmetry to asymmetry and the relatively large shear slippage along the NF plane is similar with the character of strike fault.

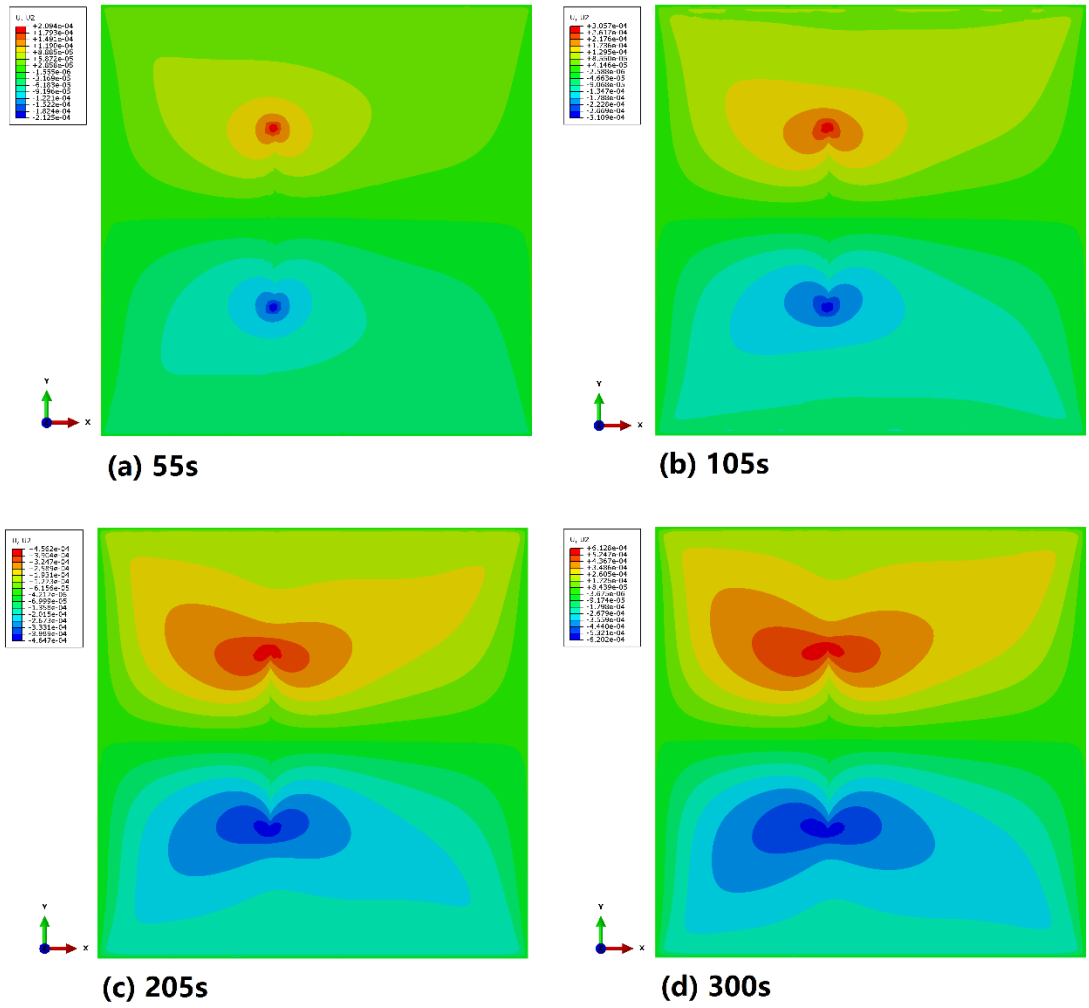


Figure 4.2 Cloud graph of y-direction displacement before intersection.
This illustrates the cloud graph of y-direction displacement before intersection. As time goes, y-direction displacement value increases, and the value is symmetrical with the wellbore.

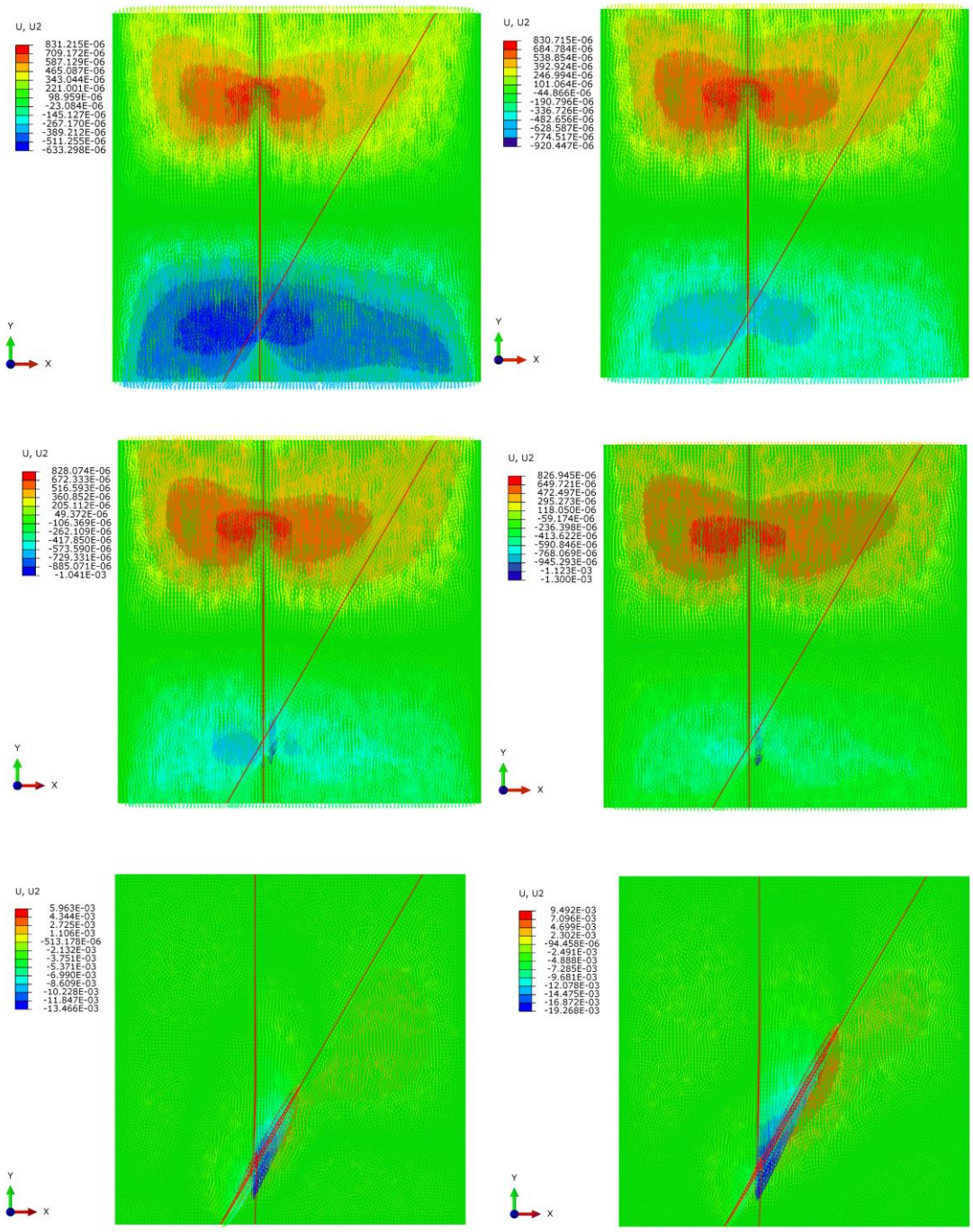


Figure 4.3 Vector graph of y-displacement during intersection at 451.7 s. The red lines represents the position of HF and NF.

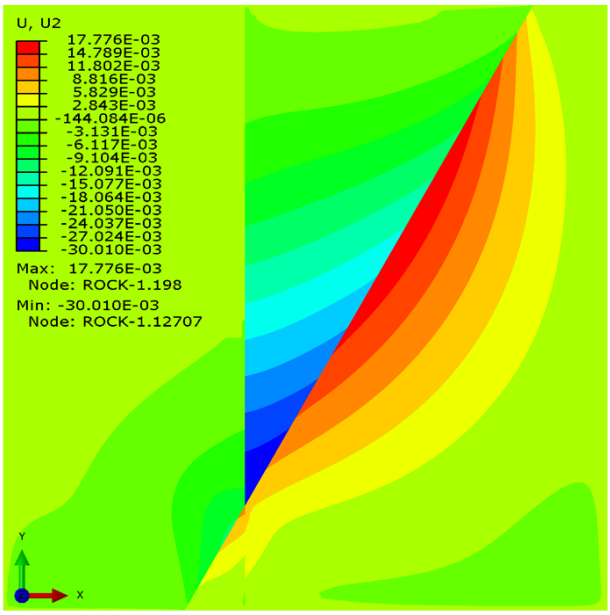


Figure 4.4 Cloud graph of y-direction displacement at 603 s after intersection.
This demonstrates the cloud graph of y-direction displacement at 603 s after intersection. There is a big displacement difference along NF, which can cause slip.

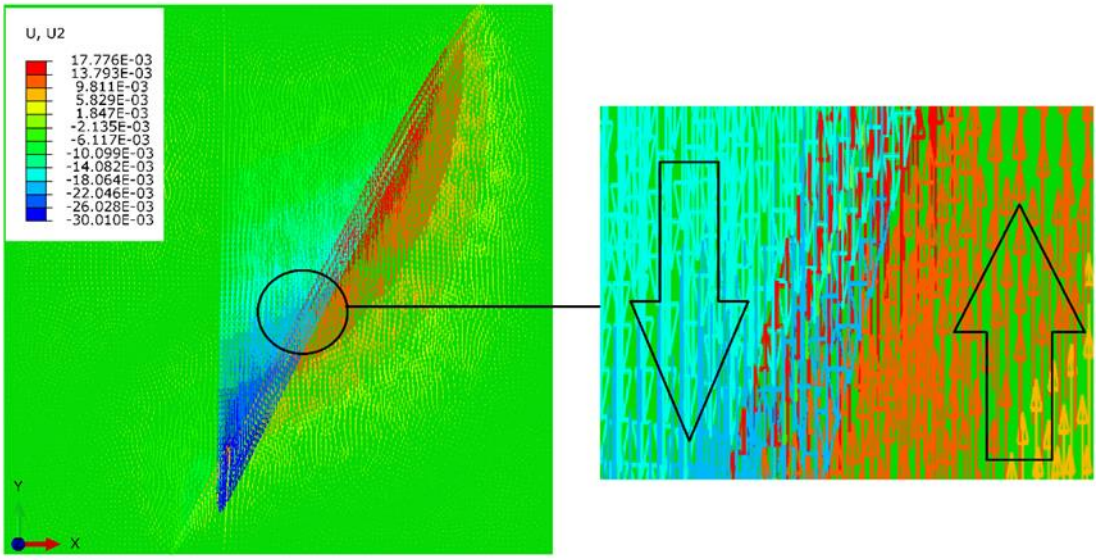


Figure 4.5 Vector graph of y-direction displacement at 603 s.
This denotes the direction of the displacement. From the zoon graph it can be tell that the formation on the left-hand side of the NF has the tendency to go down, while the formation on the left shows the trend of moving up. This relative movement will cause shear to move along NF.

The maximum y-direction displacement with injection time relation curve is presented in Figure 4.6. The detailed relation before and after formation slip are illustrated in Figure 4.7 and Figure 4.8. These figures show that before intersection or slip initiation, the y-direction slip displacement is in a magnitude of 10^{-3} to 10^{-2} mm and increases with time. Once it gets close to the critical point, the y-direction displacement sharply increases to a high magnitude of 30 mm within a short time of couple seconds. After intersection completes, the maximum y-direction displacement again increases along with time.

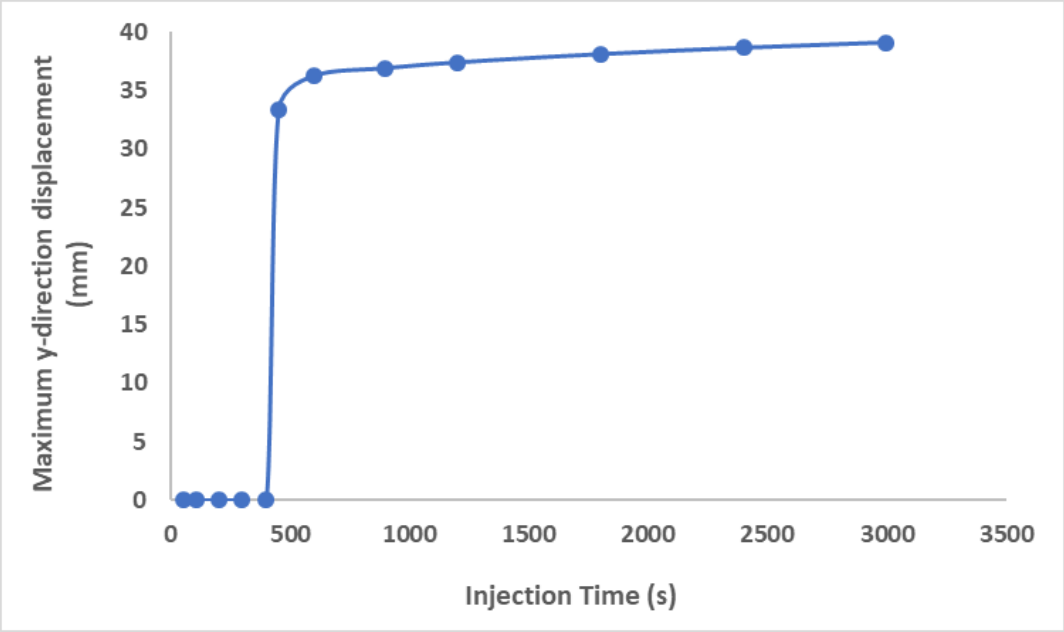


Figure 4.6 Maximum y-direction displacement changes with time.

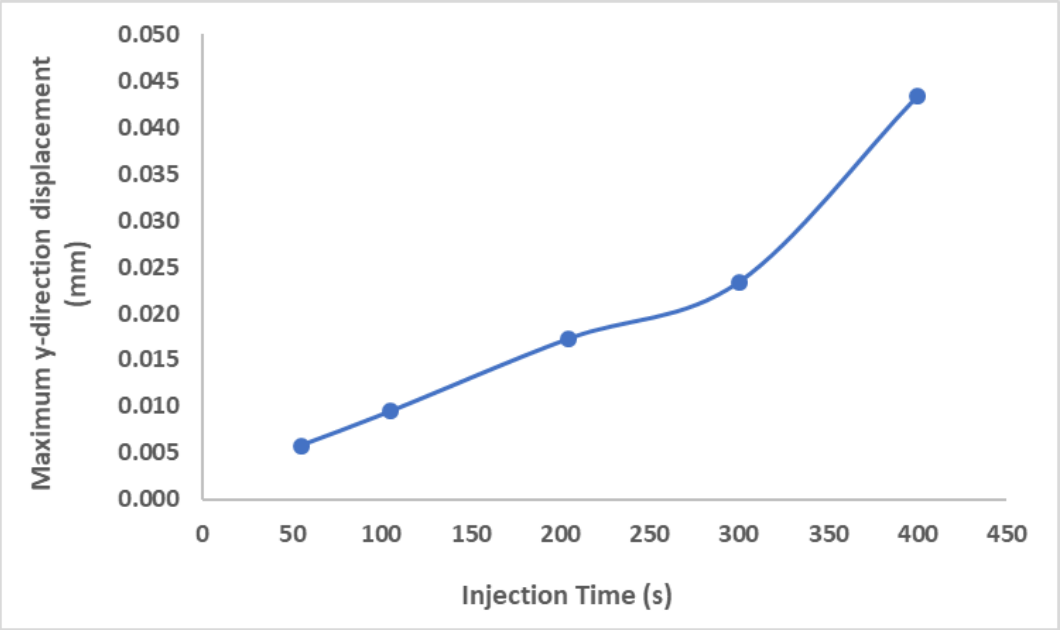


Figure 4.7 Maximum y-direction displacement before slip.

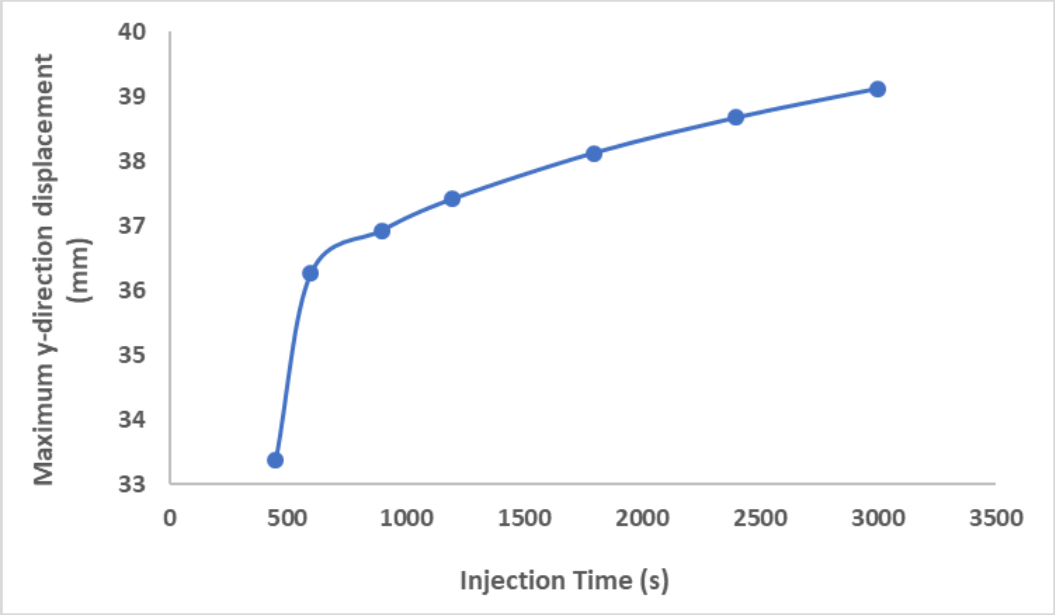


Figure 4.8 Maximum y-direction displacement after slip.

Wellbore Displacement

Figure 4.9 and Figure 4.11 are the wellbore displacement on x and y direction at different time before formation slip, while Figure 4.10 and Figure 4.12 show the displacement after slip. Table 4.2 presents the maximum y-direction value with injection time. From the displacement graph it can be told that discontinuous displacements occur at the two intersections of HF-horizontal well and NF-horizontal well, which are 40 m and 59 m. After intersection, from 40 m to 59 m, the maximum relative axial (x-direction) displacement at wellbore increases from around 2 mm to 22 mm, the maximum relative transverse (y-direction) displacement at wellbore leaps from 0 mm to 18 mm, then 30 mm. This transverse displacement of wellbore, namely rock slippage, would cause the shear deformation of casing in wellbore.

In W2X shale gas well, the type of P110 casing with an outer diameter (OD) of 127 mm was used. The formation maximum slippage value of 30 mm takes up 23.6% of the P110 grade casing OD, which has a great chance to cause casing deformation.

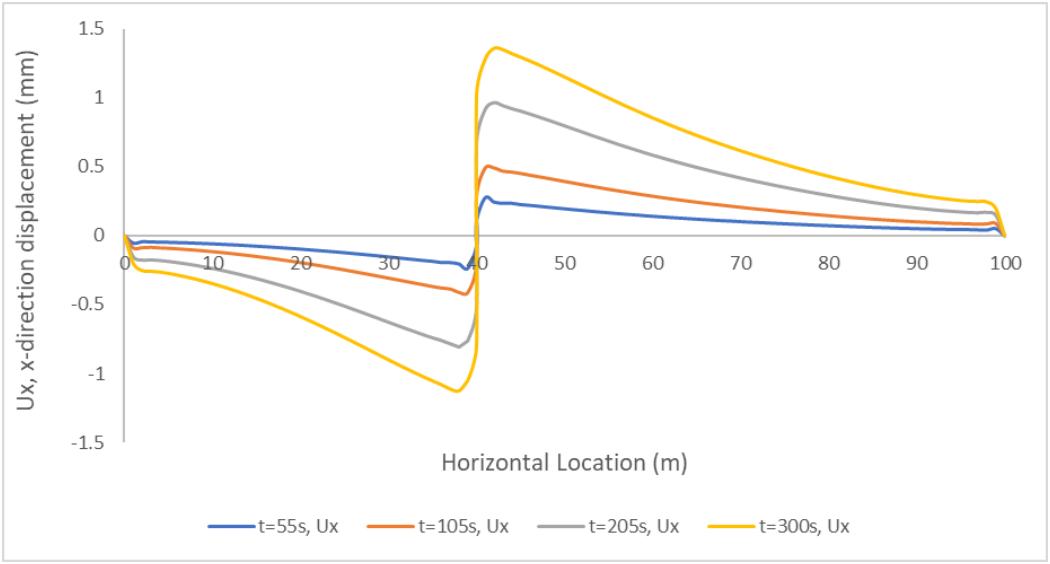


Figure 4.9 X-direction displacement along horizontal well before slip.

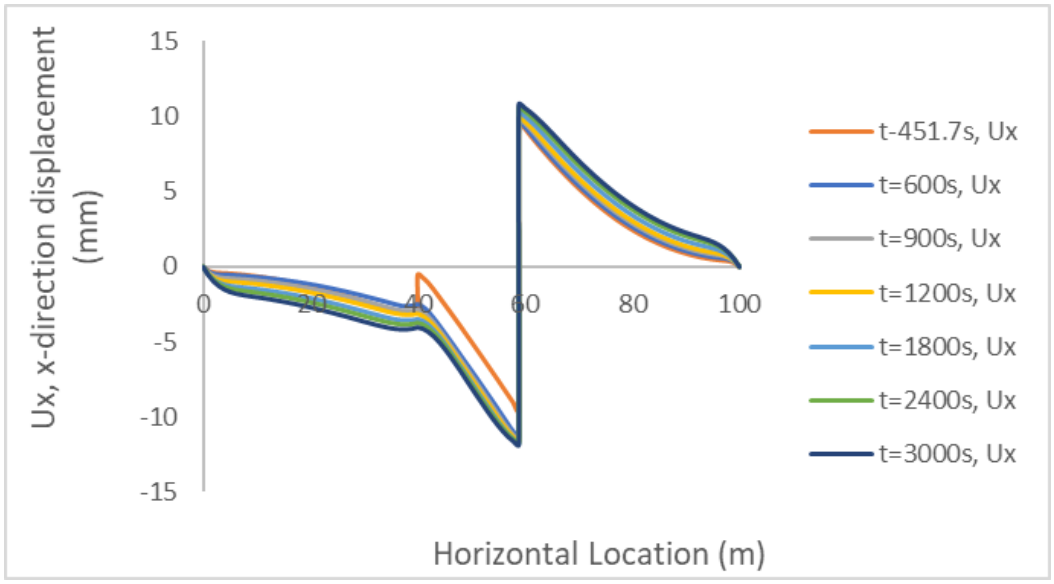


Figure 4.10 X-direction displacement along horizontal well after slip.

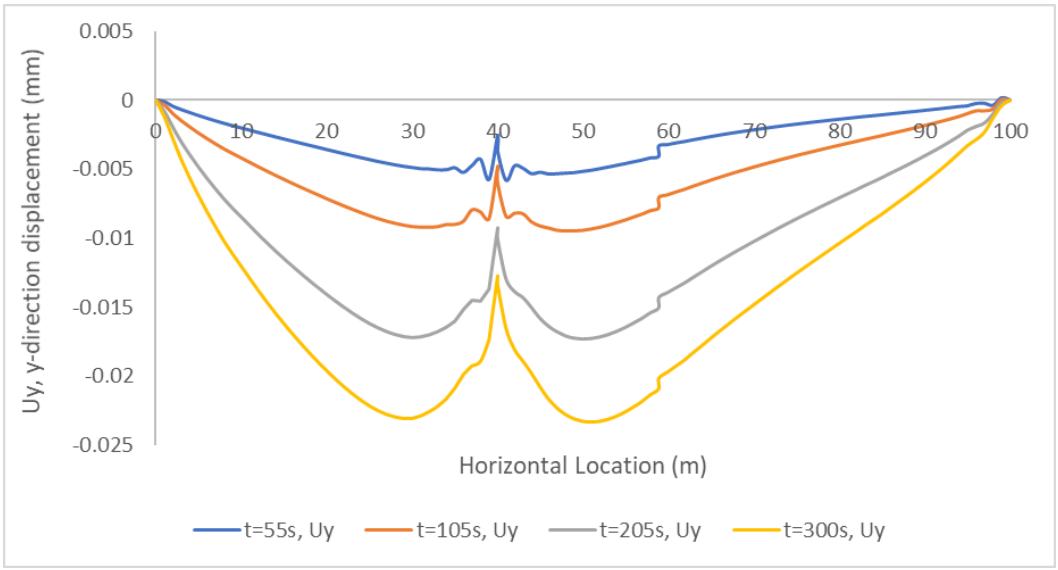


Figure 4.11 Y-direction displacement along horizontal well before slip.

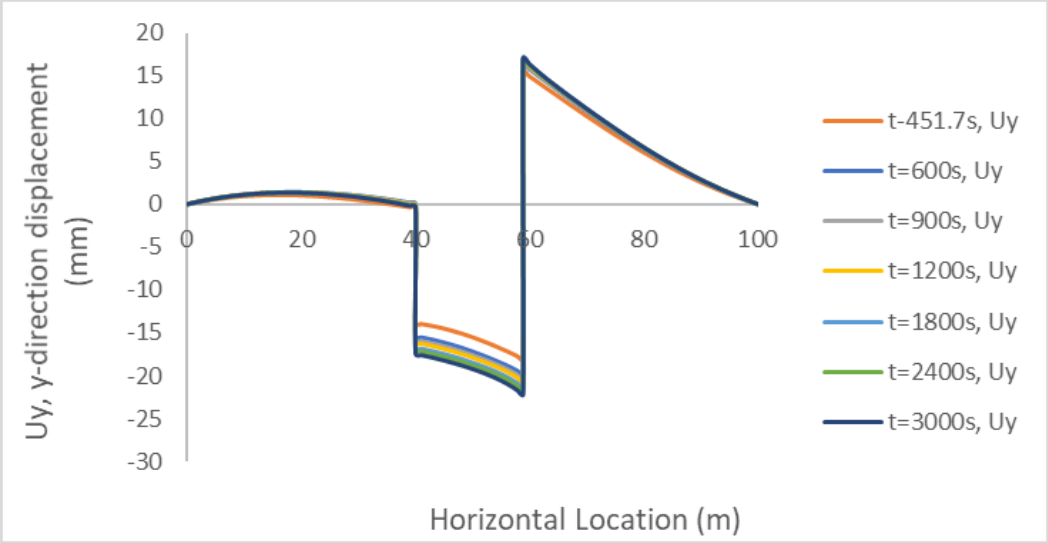


Figure 4.12 Y-direction displacement along horizontal well after slip.

Table 4.2 Maximum y-direction displacement changes with time.

Injection Time (s)	Maximum y-direction Displacement (mm)
451.7	33.391
600	36.272
900	36.930
1200	37.417
1800	38.128
2400	38.673
3000	39.121

Although the specific deform value of W2X well is unknown due to the lack of well log data. However, from the wells' data in C-W area, the magnitude of casing shear deformation is in the range of 10~50 mm, which match the simulation results.

Chapter 5: Sensitivity Study

The numerical simulation can help insight the effect of input parameters on slip displacement response and slip initiate time. When investigate the influence of one parameter, only the input value of this parameter changes, while the other parameters keep being the same as base case input. The base case input is listed below in Table 5.1.

Table 5.1 Input parameter for 2D base model simulation.

Parameter	Value	Unit
Young's modulus	30	GPa
Poisson's ratio	0.25	-
Tensile strength	2.9 (HF), 1.45 (NF)	MPa
Shear strength	20 (HF), 12 (NF)	MPa
Permeability	0.1	mD
Void Ratio	0.02	-
Critical fracture energy	30	J/m^2
Leak-off coefficient	2×10^{-12}	$m^2/s/Pa$
Fluid viscosity	1	mPa·s
Maximum horizontal stress S_H	53	MPa
Minimum horizontal stress S_h	33	MPa
Vertical stress S_v	48	MPa
Initial pore pressure	23	MPa
Injection Rate	0.00016	m^2/s
Specific weight of fluid	9800	N/m^3

5.1 Tectonic Stress

The tectonic stress in C-W area shows great value difference in horizontal plane, the uneven stress applying on casing may endanger the casing integrity and cause casing deformation. To investigate the effect of tectonic stress on slip displacement, the

horizontal tectonic stress difference is set at 0.6 MPa, 0.8 MPa, 1 MPa, 1.2 MPa, and 1.4 MPa. the rest of the parameter input are same as sensitivity study base model. The results are demonstrated in Table 5.2 and Figure 5.1. It can be concluded from the results that a higher tectonic stress difference will intensify the displacement in y-direction, which increase the chance of casing deformation from occurring. A longer injection time can also contribute to the displacement extent.

For areas with high geological heterogeneity, refinement partition of fracture can be taken. By doing so, fracturing parameters like fracturing fluid injecting rate, fracturing pressure, proppant and sand contents ratio can be adjusted to a level more suitable for each stage.

Table 5.2 Sensitivity on tectonic stress.

Horizontal stress difference (MPa)	**Maximum y-direction Displacement after 30 min (mm)**	**Maximum y-direction Displacement after 40 min (mm)**	**Maximum y-direction Displacement after 50 min (mm)**
0.6	7.03	7.27	7.41
0.8	10.21	10.49	10.69
1	12.75	13.07	13.311
1.2	15.36	15.73	16.01
1.4	18.01	18.43	18.74

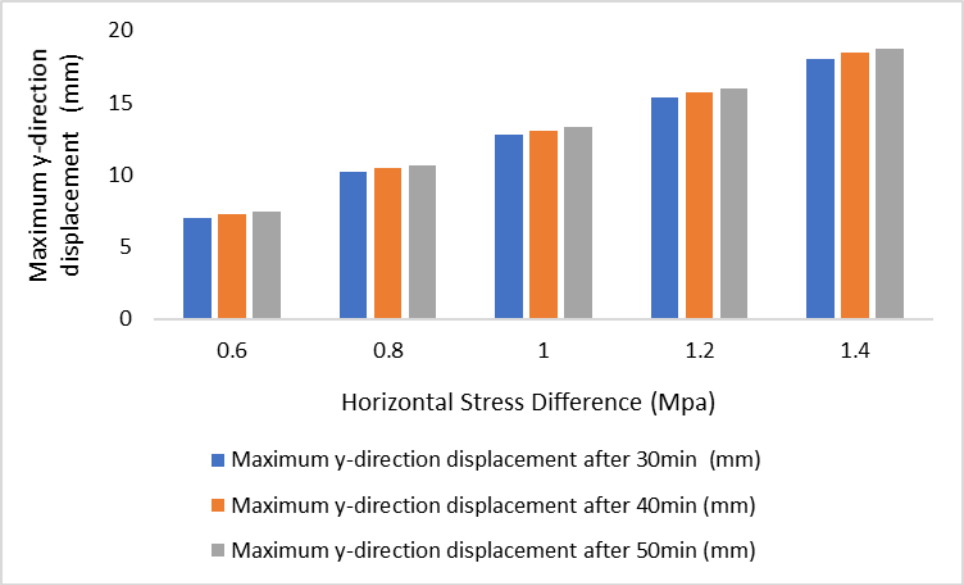


Figure 5.1 Influence rule of tectonic stress difference on slip displacement.

5.2 Young's Modulus

Young's modulus (YMS) describes the ability of a solid material to withstand tension or compression, which is an indicator of rock elastic properties. To understand the relation between YMS and formation y-direction displacement, a set of YMS of 25 MPa, 30 MPa, 35 MPa, 40 MPa, and 45 MPa are used to run simulation. The relation curve and the result details are depicted in Figure 5.2 and Table 5.3.

The simulation results show that the maximum y-direction displacement value decreases as YMS increases because a larger YMS represents a higher ability to withstand stress, which means that formation is stiffer and will show less deformation under the same stress.

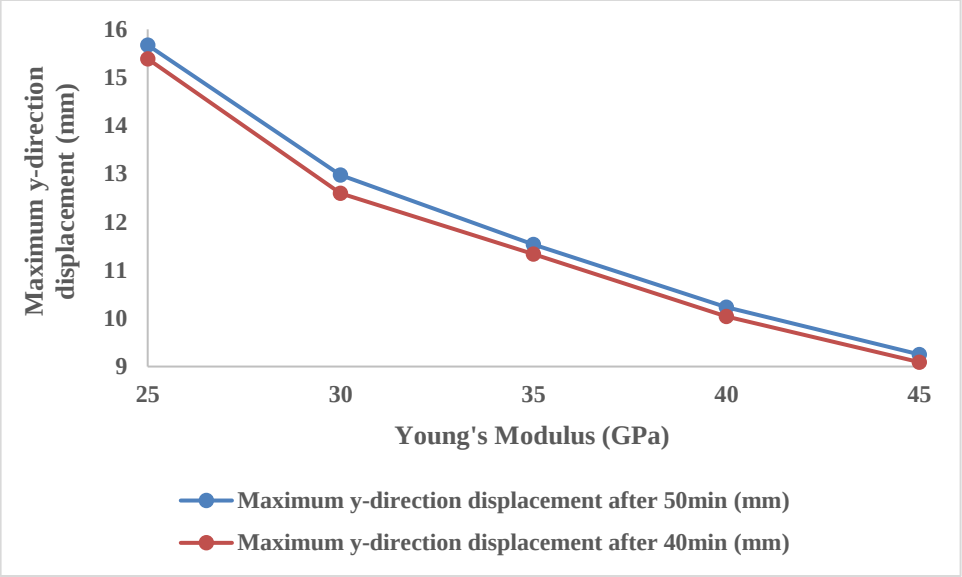


Figure 5.2 Maximum y-direction displacement and YMS relation curve.

Table 5.3 Maximum y-direction displacement under different Young's Modulus.

Young's Modulus (GPa)	Maximum y-direction displacement after 50 min (mm)	Maximum y-direction displacement after 40 min (mm)
25	15.67	15.39
30	12.97	12.60
35	11.54	11.33
40	10.23	10.04
45	9.25	9.09

5.3 Fracturing Fluid Injection Rate

When choosing casing, Miskimins (2008) stressed the importance of maximum treatment pressure and rates, treatment staging, and liquid loading.

As presented in Figure 5.3 as the injection rate decreases form right to left, the slippage initiate time increases. From Figure 5.4, maximum y-direction displacement will increase with injection time and injection rate. The simulation result details are listed in Table 5.4.

Following this trend, when the slip initiate time equals is larger than or equal to the injection time, no slip will occur. However, the injection rate under this condition might not be enough for fracturing. To balance the slip initiate time, the maximum shear displacement with injection rate is should be studied in the future work.

Control fracturing fluid pressure can prevent the slippage of formation along natural fracture. However, due to the unclear understanding of the natural fracture, stratigraphic interface and fault properties, the theoretical critical injecting flow rate cannot be given yet.

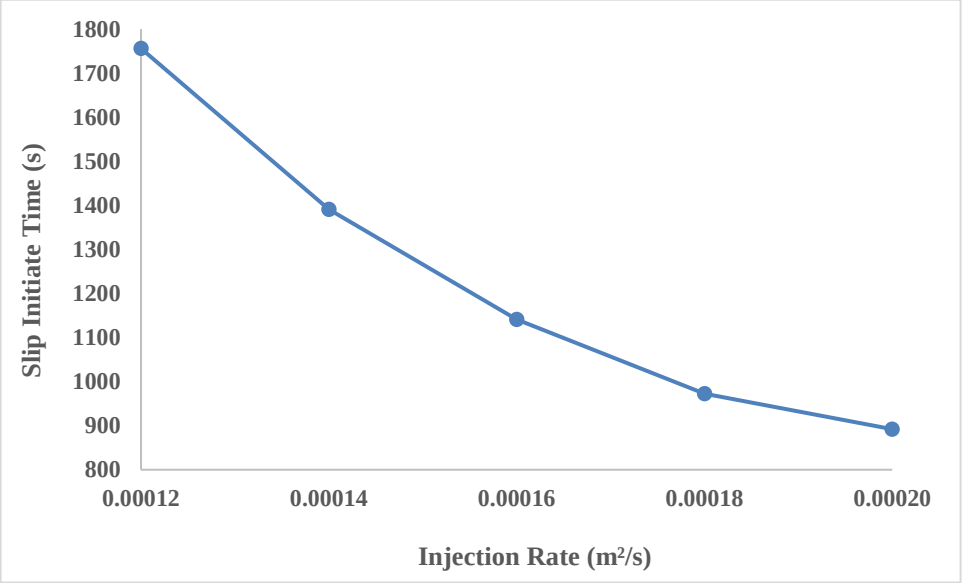


Figure 5.3 Slippage initiate time with injection rate.

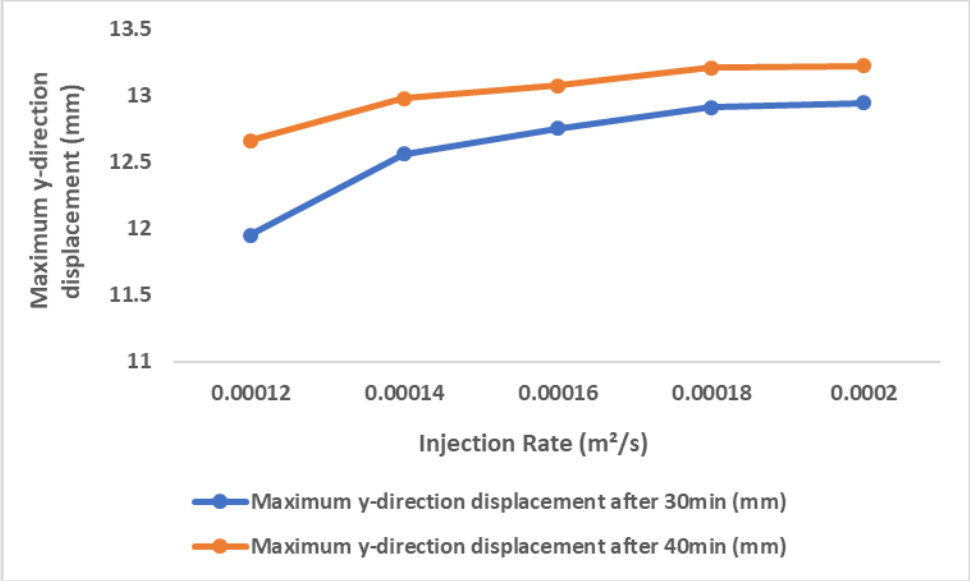


Figure 5.4 Maximum y-direction displacement under different injection rate.

Table 5.4 Slip response under different injection rate.

Injection Rate (m^2/s)	Maximum y-direction Displacement after 30 min (mm)	Maximum y-direction Displacement after 40 min (mm)	Slip Initiate Time (s)
0.00012	11.95	12.66	1756
0.00014	12.56	12.98	1391
0.00016	12.75	13.07	1141
0.00018	12.91	13.21	972
0.0002	12.94	13.22	892

5.4 Fracturing Fluid Viscosity

In field, the fracturing fluid viscosity greatly affects the fluid rheological property, shear stability, proppant-carrying ability and leak-off rate. To figure out the relation between fracturing fluid viscosity and formation slip, based on base model, three different viscosities of 0.1 mPa·s, 0.4 mPa·s, 0.8 mPa·s are chosen for study. Simulation results is depicted in Figure 5.5 and data details are summarized in Table 5.5. From the result, it is

obvious that maximum shear displacement rises with viscosity and time incensement, while the rates of rise both decreases.

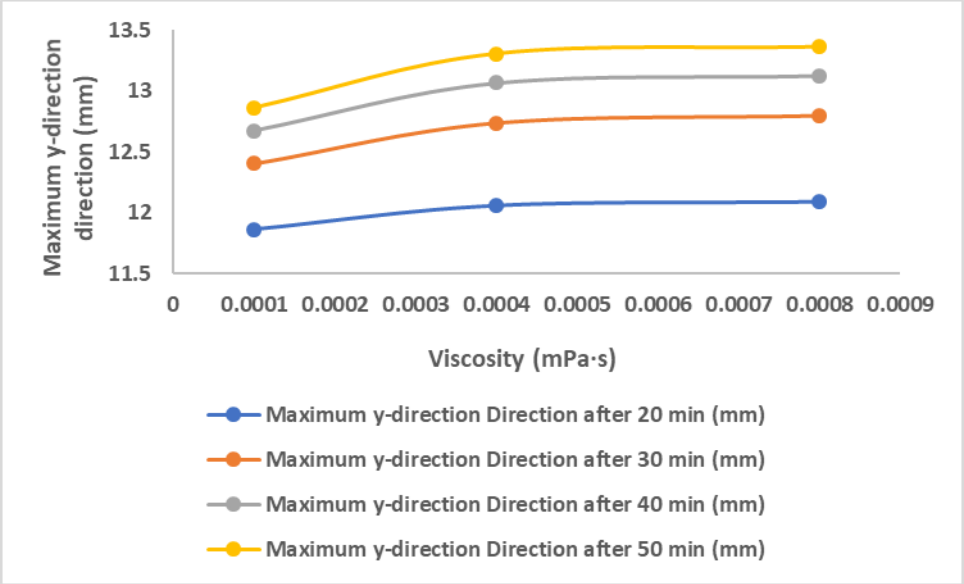


Figure 5.5 Maximum y-direction displacement under different viscosity.

Table 5.5 Slip situation under different viscosity.

Viscosity (mPa·s)	Maximum y-direction Displacement after 20 min (mm)	Maximum y-direction Displacement after 30 min (mm)	Maximum y-direction Displacement after 40 min (mm)	Maximum y-direction Displacement after 50 min (mm)
0.0001	11.862	12.403	12.671	12.861
0.0004	12.056	12.734	13.066	13.306
0.0008	12.087	12.794	13.126	13.362

Chapter 6: Conclusions and Recommended Future Work

In this thesis, the casing deformation mechanism is studied by developing a 2D coupled hydro-mechanical model for modeling formation response and casing deformation during hydraulic fracturing. HF-NF intersecting and formation slippage occurrences are simulated in the case study of C-W shale gas play. Parametric sensitivity analysis is used to investigate the influencing factors. Based on this research, the key conclusions are drawn as follows:

(1) The pre-existing natural fractures or faults can lead to casing deformation during hydraulic fracturing because of formation shear slip in shale reservoir;
(2) This simplified 2D coupled hydro-mechanical model can model the pore pressure, stress fields, fracture open width, slip displacement, and casing deformation in fractured formation;
(3) Casing failure in C-W shale plays can be caused by formation deformation and natural fracture slippage;
(4) In practice, the 2D model can be used to simulate scenarios under real treatment condition to guide the casing design;
(5) The excessive differential tectonic stress, injection rate, and injection fluid viscosity increases slip displacement of natural fracture;
(6) A larger Young's Modulus value means a higher rock stiffness and rock have better ability to withstand shear stress.

Suggestions can be given according to the simulation results: Even though tectonic stress anisotropy is inevitable, geological data analysis can help detect and avoid

big tectonic stress different areas and areas with weak planes. Controlling injection rate and fluid selection can help reducing slip risk.

For future work, three major work contents are planning to be performed:

(1) Build a 3D model containing cement and casing to get more detailed casing behavior during fracturing;

(2) Add temperature field in the model. Temperature fluctuates significantly during fracturing and can change the casing stress state, which is believed to be an influencing factor (Tian, Shi et al. 2015);

(3) Field measurement and validation. To verify the accuracy of this model, obtain more information like well log interpretation about casing deform sections and compare with the simulation results with this 2D Model to get a more solid model validation and practical meaning. If the predicted results are consistent with the logging data, this model can be solid verified.

References

Bao, X. and D. W. Eaton (2016). "Fault activation by hydraulic fracturing in western Canada." Science: aag2583.

Barenblatt, G. I. (1962). The Mathematical Theory of Equilibrium Cracks in Brittle Fracture. Advances in Applied Mechanics. H. L. Dryden, T. von Kármán, G. Kuerti, F. H. van den Dungen and L. Howarth, Elsevier. **7:** 55-129.

Benzeggagh, M. and M. Kenane (1996). "Measurement of mixed-mode delamination fracture toughness of unidirectional glass/epoxy composites with mixed-mode bending apparatus." Composites science and technology **56**(4): 439-449.

Bruno, M. S. (2001). Geomechanical Analysis and Decision Analysis for Mitigating Compaction Related Casing Damage. SPE Annual Technical Conference and Exhibition. New Orleans, Louisiana, Society of Petroleum Engineers.

Camanho, P. P. and C. G. Dávila (2002). "Mixed-mode decohesion finite elements for the simulation of delamination in composite materials."

Chen, Z., L. Shi and D. Xiang (2017). "Mechanism of casing deformation in the Changning–Weiyuan national shale gas demonstration area and countermeasures." Natural Gas Industry B **4**(1): 1-6.

Chipperfield, S. T., J. R. Wong, D. S. Warner, C. L. Cipolla, M. J. Mayerhofer, E. P. Lolon and N. R. Warpinski (2007). "ShEaR DiLaTioN DiagNoSTiCS—a NEW aPPRoaCh foR EvaLuaTiNg TighT gaS STiMuLaTioN TREaTMENTS." The APPEA Journal **47**(1): 221-238.

Chong, Z., X. Li and X. Chen (2017). "Effect of Injection Site on Fault Activation and Seismicity during Hydraulic Fracturing." Energies **10**(10): 1619.

Council, G. W. P. (2009). Modern shale gas development in the United States: A primer, na.

Council, N. R. (2013). Induced seismicity potential in energy technologies, National Academies Press.

Daneshy, A. A. (2005). Impact of Off-Balance Fracturing on Borehole Stability and Casing Failure. SPE Western Regional Meeting. Irvine, California, Society of Petroleum Engineers.

Davies, R. J., S. Almond, R. S. Ward, R. B. Jackson, C. Adams, F. Worrall, L. G. Herringshaw, J. G. Gluyas and M. A. Whitehead (2014). "Oil and gas wells and their integrity: Implications for shale and unconventional resource exploitation." Marine and Petroleum Geology **56**: 239-254.

Drucker, D. C. and W. Prager (1952). "Soil mechanics and plastic analysis or limit design." Quarterly of applied mathematics **10**(2): 157-165.

Dugdale, D. S. (1960). "Yielding of steel sheets containing slits." Journal of the Mechanics and Physics of Solids **8**(2): 100-104.

Dusseault, M. B., M. S. Bruno and J. Barrera (2001). "Casing Shear: Causes, Cases, Cures."

Furui, K., G.-F. Fuh, N. A. Abdelmalek and N. Morita (2010). "A Comprehensive Modeling Analysis of Borehole Stability and Production-Liner Deformation for Inclined/Horizontal Wells Completed in a Highly Compacting Chalk Formation."

Geertsma, J. and F. De Klerk (1969). "A Rapid Method of Predicting Width and Extent of Hydraulically Induced Fractures."

Guo, J., B. Luo, C. Lu, J. Lai and J. Ren (2017). "Numerical investigation of hydraulic fracture propagation in a layered reservoir using the cohesive zone method." Engineering Fracture Mechanics **186**: 195-207.

Haddad, M. and K. Sepehrnoori (2015). "Simulation of hydraulic fracturing in quasi-brittle shale formations using characterized cohesive layer: Stimulation controlling factors." Journal of Unconventional Oil and Gas Resources **9**: 65-83.

Haddad, M. and K. Sepehrnoori (2015). Simulation of hydraulic fracturing in quasi-brittle shale formations using characterized cohesive layer: Stimulation controlling factors.

Hughes, T. J. (2012). The finite element method: linear static and dynamic finite element analysis, Courier Corporation.

Ingraffea, A. R., M. T. Wells, R. L. Santoro and S. B. Shonkoff (2014). "Assessment and risk analysis of casing and cement impairment in oil and gas wells in Pennsylvania, 2000–2012." Proceedings of the National Academy of Sciences **111**(30): 10955-10960.

Kuuskraa, V. A., S. Stevens and K. Moodhe (2013). "EIA/ARI world shale gas and shale oil resource assessment." Arlington, VA and Washington, DC **17**: 14.

Lian, Z., H. Yu, T. Lin and J. Guo (2015). "A study on casing deformation failure during multi-stage hydraulic fracturing for the stimulated reservoir volume of horizontal shale wells." Journal of Natural Gas Science and Engineering **23**(Supplement C): 538-546.

Maxwell, S. C., T. I. Urbancic, N. Steinsberger and R. Zinno (2002). Microseismic Imaging of Hydraulic Fracture Complexity in the Barnett Shale. SPE Annual Technical Conference and Exhibition. San Antonio, Texas, Society of Petroleum Engineers.

Miskimins, J. L. (2008). Design and Life Cycle Considerations for Unconventional Reservoir Wells. SPE Unconventional Reservoirs Conference. Keystone, Colorado, USA, Society of Petroleum Engineers.

Moës, N., J. Dolbow and T. Belytschko (1999). "A finite element method for crack growth without remeshing." International journal for numerical methods in engineering **46**(1): 131-150.

Munjiza, A. A. (2004). The combined finite-discrete element method, John Wiley & Sons.

Nasiri, A. (2015). A Comparison Study of KGD, PKN and a Modified P3D Model.

National Academies Press issuing, b. and i. b. National Research Council . Committee on Induced Seismicity Potential in Energy Technologies (2013). Induced seismicity potential in energy technologies, Washington, DC : National Academies Press.

Nierode, D. (1985). "Comparison of hydraulic fracture design methods to observed field results." Journal of petroleum technology **37**(10): 1,831-831,839.

Nordgren, R. P. (1972). "Propagation of a Vertical Hydraulic Fracture."

Roberts, D. L. (1953). Shear Prevention in the Wilmington Field. Drilling and Production Practice. New York, New York, American Petroleum Institute.

Rutqvist, J., A. P. Rinaldi, F. Cappa and G. J. Moridis (2013). "Modeling of fault reactivation and induced seismicity during hydraulic fracturing of shale-gas reservoirs." Journal of Petroleum Science and Engineering **107**: 31-44.

Systèmes, D. (2014). "Abaqus Analysis User's Guide." Solid (Continuum) Elements **6**.

Terzaghi, K., R. B. Peck and G. Mesri (1996). Soil mechanics in engineering practice, John Wiley & Sons.

Tian, Z., L. Shi and L. Qiao (2015). "Problems in the wellbore integrity of a shale gas horizontal well and corresponding countermeasures." Natural Gas Industry B **2**(6): 522-529.

Tiejun, L., Y. Hao, L. Zhanghua and S. Biao (2017). "Casing failure mechanism during volume fracturing: A case study of shale gas well." Advances in Mechanical Engineering **9**(8): 1687814017717182.

Tjengdrawira, M. A., A. Khaksar, S. H. Ong, R. I. Sjari'at and A. Suhadi (2017). Geomechanical Study at An Onshore Central Sumatra Field: The Investigation of Casing Restriction and Deformation in Shallow Sand Formation. SPE/IATMI Asia Pacific Oil & Gas Conference and Exhibition, Society of Petroleum Engineers.

Wang, H., H. Liu, H. A. Wu and X. X. Wang (2015). "A 3D numerical model for studying the effect of interface shear failure on hydraulic fracture height containment." Journal of Petroleum Science and Engineering **133**: 280-284.

Yan, W., H. Ge, J. Wang, D. Wang, F. Meng, J. Chen, X. Wang and N. J. McClatchey (2016). "Experimental study of the friction properties and compressive shear failure behaviors of gas shale under the influence of fluids." Journal of Natural Gas Science and Engineering **33**: 153-161.

Yin, F., L. Han, S. Yang, Y. Deng, Y. He and X. Wu (2018). "Casing deformation from fracture slip in hydraulic fracturing." Journal of Petroleum Science and Engineering **166**: 235-241.